

## Artificially thickened boundary layer turbulence due to trip wires of varying diameter

Zhanqi Tang<sup>1</sup>,<sup>2</sup>,\* Nan Jiang,<sup>1,2</sup> Zhiming Lu,<sup>3</sup> and Quan Zhou<sup>3</sup>

<sup>1</sup>*Department of Mechanics, Tianjin University, Tianjin 300350, China*

<sup>2</sup>*Tianjin Key Laboratory of Modern Engineering Mechanics, Tianjin 300350, China*

<sup>3</sup>*Shanghai Key Laboratory of Mechanics in Energy Engineering, Shanghai Institute of Applied Mathematics and Mechanics, School of Mechanics and Engineering Science, Shanghai University, Shanghai 200072, China*



(Received 29 September 2023; accepted 1 February 2024; published 26 February 2024)

In this paper, we study the artificially thickened boundary layer flows downstream of the tripping configuration that consists of a set of trip wires of varying diameters. Single-point hot-wire measurements are executed at a fixed streamwise location in the adaptation region, where the boundary layer is in conditions ranging from understimulation to overstimulation. Comparisons of the mean flow, Reynolds stress, energy spectra, and higher-order turbulence statistics demonstrate that the tripping effects are significant in the outer region, by introducing the enhanced energetic large scales with increasing the trip-wire diameter. The emergence of large scales manifests the scale separation in the overstimulated conditions, implying that the boundary layer has the potential to simulate high-Reynolds-number flows in the current tripping configurations. Then we attempt to identify the effect of the emergent large scales by examining the scale interactions. Under the overstimulated conditions, the generated large-scale structures penetrate down to the wall and superimpose energy in the near-wall region. The cross-term of the scale-decomposed skewness factor reveals that the amplitude modulation (AM) of the large scales on small scales is enhanced in the near-wall region. On the other hand, the frequency modulation (FM) is discussed by the zero-crossings-based evidence. Both the AM and FM effects become more significant with increasing the trip-wire diameter and the free-stream velocity. Far away from the wall, a reversal mechanism occurs and becomes more noticeable due to the tripping influence on the external intermittency. Moreover, it is found that the intermittent geometry of the turbulent/nonturbulent interface exhibits a fractallike self-similar convolution behavior in the current artificially thickened wall turbulence.

DOI: [10.1103/PhysRevFluids.9.024606](https://doi.org/10.1103/PhysRevFluids.9.024606)

### I. INTRODUCTION

In some respects, the turbulent boundary layer (TBL) flow is characterized by a competition between inertial and viscous forces, quantified by the Reynolds number. The friction Reynolds number is defined as  $Re_\tau = u_\tau \delta / \nu$ , where  $u_\tau$  is the friction velocity,  $\delta$  is the boundary layer thickness, and  $\nu$  is the kinematic viscosity. Here,  $Re_\tau$  can be interpreted as the ratio of two motion scales: the largest eddies at the characteristic length scale of boundary layer thickness  $\delta$  and the smallest eddies characterized at the viscous length scale  $\nu/u_\tau$ . As  $Re_\tau$  increases, it is argued that turbulent motions with different scales perform in their full form as they should. Over the past decades, considerable progress has been made in understanding the Reynolds number dependence of

\*zhanqitang@tju.edu.cn

TBL flows from diverse perspectives [1,2], including turbulence statistics [3,4], organized structures [5], and scale interactions [4,6–9].

Considering the engineering applications, there is an existing difference in TBL flows between the academic and engineering communities. For turbulent flows in wind turbines, pipelines, ships, and aviation, the typical values of the Reynolds number are in the range of  $Re_\tau \approx 4000$ – $6000$  to  $10\,000$ – $100\,000$ , which is higher than the flows that can be commonly achieved through laboratory experiments or direct numerical simulations (DNSs). High- $Re_\tau$  flows have attracted more and more attention worldwide. However, the construction of high- $Re_\tau$  facilities poses both infrastructural and financial challenges. Therefore, it is desirable to explore more economical and feasible approaches to generate high- $Re_\tau$  TBL flows.

The characteristic velocity and length,  $u_\tau$  and  $\delta$ , are two common parameters to be considered to increase  $Re_\tau$  of TBL flows. Generally, increasing the free-stream velocity results in a growth of  $u_\tau$  but leads to a decrease of viscous length scale  $\nu/u_\tau$ , which will increase the challenge to the spatial/temporal resolution of experiments and simulations. As a characteristic length, the boundary layer thickness  $\delta$  slowly increases with the development of TBL flow, which means that it is necessary to have an exceptionally long test section to achieve an expected  $\delta$  [10]. Hence, for a wind tunnel with the given test section length, it is more desirable to artificially thicken  $\delta$  via the tripping configuration at the leading edge, for the achievement of a higher  $Re_\tau$  TBL flow.

In their pioneering work, Klebanoff and Diehl [11] utilized a set of different trips to artificially thicken the boundary layer, which indicates that the initial condition at the leading edge has a significant impact on the development of boundary layer flows. Subsequent investigations have corroborated that the minor modification of the trip parameters can engender noncanonical TBL up to surprisingly high  $Re_\tau$  (high  $\delta$ ) in the adaptive region [12,13]. These findings suggest that the introduction of perturbations via tripping devices at the leading edge is an accepted approach for attaining higher- $Re_\tau$  TBL flows. Considerable efforts have been dedicated to understanding the effects of the exact tripping devices with different sizes and shapes on the evolution of boundary layers. Erm and Joubert [14] revealed the influence of various tripping conditions on TBLs, such as cylinder wire, distributed grit, and cylindrical pins. They concluded that a certain free-stream velocity requires a unique tripping device to form a desirable TBL flow. By an elaborately appropriate trip design, Rodríguez-López *et al.* [15] employed two families of tripping devices (i.e., high-aspect-ratio uniform distributed cylinders and low-aspect-ratio sawtooth fence) to artificially generate higher- $Re_\tau$  TBLs. Correspondingly, it was argued that the boundary layer is generated by the wall- and wake-driven mechanisms. For the wall-driven mechanism, the inner structures drive the mixing of the tripping wake with the wall-bounded flow. On the other hand, the wake-driven mechanism is related to a long adaptation region, in which the inner structures are reorganized under the wake influence. The two kinds of driven mechanisms were further discussed by considering the different geometric configurations [16,17]. Moreover, Marusic *et al.* [10] measured the spatial development of high- $Re_\tau$  TBL flows and observed the scaling behaviors from different tripping conditions, which include standard sandpaper and threaded rods of different diameters. They reported that a significant difference can be noted in the outer region due to the introduction of large-scale disturbances by the trips, and the memory of this overtripped effect exceeds 10 m along the streamwise direction. This finding was further supported by Sanmiguel Vila *et al.* [18] based on the high-fidelity DNS and experimental data. They explored different tripping configurations ranging from undertripped to overtripped conditions and verified that the overtripped case leads to more prominent wake flows.

To sum up, it is evident that, within a finite-length test section, the geometry of the tripping devices plays a dominant role in determining the turbulence behavior of artificially thickened boundary layer flows. Nevertheless, the specific structures dominating the adaptive region and their impact on the scale interaction and arrangement are less investigated. Furthermore, the influence of tripping configuration on the boundary layer flows still lacks comprehensive understanding, owing to the diverse array of tripping conditions. In this paper, we utilize transverse cylindrical rods as the trip wires, each with progressively increasing diameters, to systematically induce artificially

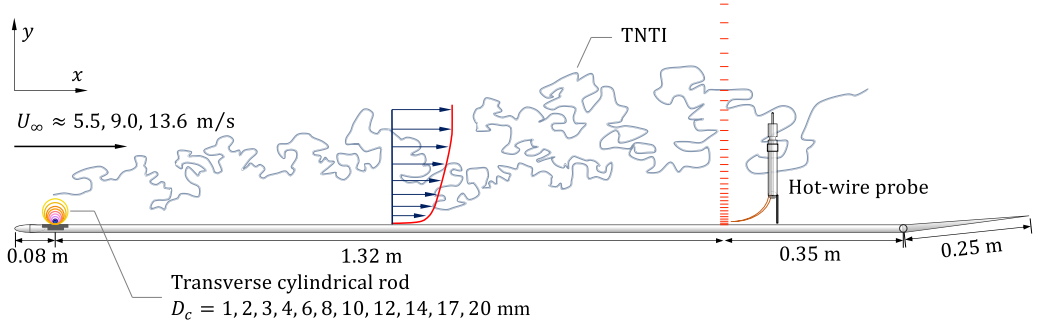


FIG. 1. Sketch of the hot-wire experimental setup and trip wires of varying diameters.

thickened boundary layer flows in a finite-length wind tunnel test section. In this paper, we aim to examine the new-generated structures and their impact on statistical deviation, scale interactions, and intermittency properties within the artificially thickened TBLs under the trip-wire effects. The experimental methods are introduced in Sec. II. The basic statistics under the tripping effect are presented in Sec. III, which includes mean flow, second-order statistics including spectra, and high-order statistics. The zero-crossings-based frequency modulation (FM) will be exhibited in Sec. IV, and the self-similar intermittency in the outer region under the tripping impacts will be examined in Sec. V. Finally, the conclusions are drawn in Sec. VI.

## II. EXPERIMENTAL SETUP AND METHODS

Experiments were conducted in a closed-circuit wind tunnel at Tianjin University, as described in previous studies [19–21]. The test section of the tunnel was 2.0 m long, 0.6 m tall, and 0.8 m wide. A smooth boundary-layer plate was vertically fastened at the test section. The flat plate had a size of  $1.75 \times 0.6 \times 0.015$  m (length  $\times$  width  $\times$  thickness) within a 4:1 elliptical leading edge and was vertically fastened at the test section. A 0.25-m-long adjustable trailing-edge flap was included to control the circulation around the boundary layer plate such that the leading-edge stagnation point was located on the measurement side of the leading edge. Static wall pressure was monitored at four pressure ports spaced along the streamwise direction (0.7, 1.0, 1.25, and 1.5 m downstream of the leading edge) using an inclined-tube micromanometer. The coefficient of pressure  $C_p$  along the working section was constant to within  $\pm 0.82\%$ , consistent with conditions observed in the previous investigations [10,21]. In the present experiments, three different free-stream velocities were employed  $U_\infty \approx 5.5, 9.0$ , and  $13.6$  m/s.

The trip wire of different diameters  $D_c = 1, 2, 3, 4, 6, 8, 10, 12, 14, 17$ , and  $20$  mm was employed as the tripping device, which was mounted at the position  $80$  mm downstream of the leading edge of the plate. These cylindrical rods were fabricated from ceramic zirconia materials with high hardness and toughness. Each cylindrical rod was affixed onto a metal insert using the double-sided tape (tesa 4972), allowing the insert to be bolted into a recess in the flat plate, ensuring its surface remained flush with the plate wall. To enhance the stability of the fixed cylindrical rod, both ends of the trip were secured with glass cement, which is unlikely to introduce additional perturbations into boundary layer flows. Additionally, the case with no tripping device ( $D_c = 0$ ) was also executed. Notably, these trip wires with increasing diameter ( $D_c = 0$ – $20$  mm) were assumed to progressively stimulate the boundary layer from understimulation to overstimulation, which provides a comprehensive insight into the influence of the trip wires on the boundary layer flows.

Hot-wire measurements were carried out in the boundary layer flows. Boundary-layer traverses were conducted at the streamwise location downstream of the tripping device at  $x = 1.32$  m. The sketch of the hot-wire experimental setup is plotted in Fig. 1. A miniature single-sensor boundary layer probe (TSI-1621A-T1.5) was used with a constant temperature anemometer system

of IFA-300 operating at an overheat ratio of 1.7. The tungsten (platinum-coated) hot wire has a sensitive length of 1.25 mm and a diameter of 4  $\mu\text{m}$ , resulting in a length-to-diameter ratio ( $l/d$ ) of  $>200$  [22,23]. In terms of spatial resolution, the viscous-scaled wire length is  $l^+ < 48$  for all the measurement cases. On the other hand, Hutchins *et al.* [23] suggested that there is negligible energy content for  $f_T^+ > \frac{1}{3}$  ( $f_T^+ = f_T \nu / u_\tau^2$ , where  $f_T$  is the frequency of turbulent fluctuations). Following this suggestion, the sampling frequency for all the experimental cases was set up, and the corresponding nondimensional sample interval was  $\Delta t^+ < 0.5$  ( $\Delta t^+ = \Delta t u_\tau^2 / \nu$ , where  $\Delta t = 1/f$  and  $f$  is the sampling frequency). Note that the current sampling frequency is higher than the frequency limit of the current hot-wire probe [24]. Calibration was employed by Air Velocity Calibrator Model 1127 of IFA-300 over a velocity range of 0–22 m/s. The hot-wire probe was systematically translated to all experimental locations using a computer-controlled translation stage. Specifications of experimental parameters and trip wires are given in Table I. In the table, L, M, and H denote the low, medium, and high free-stream velocities, respectively. Due to the limit on the amount of memory, the sample length of the signals in each case was correspondingly changed with the given sampling frequency. For all the measurements, the sample length included no less than 8500 boundary-layer turnover time, even at the most thickened boundary-layer cases, which adequately covers the energy contained in the largest scales and acquires the converged statistics. Due to the tripping effects, the number of wall-normal measurement stations with logarithmical spacing was increased as the boundary layer was thickened. In addition, we monitored the probe sensor of the hot wire and adjusted for the wall-normal offset by a digital microscope-based procedure.

In this paper, the friction velocity  $u_\tau$  was estimated from the raw mean velocity profiles using a composite profile fitting approach, as outlined in the methodology of Rodríguez-López *et al.* [25]. This fitting procedure yielded not only the skin-friction velocity  $u_\tau$  but also other integral quantities such as Coles' wake strength  $\Pi$ , which will be discussed in the subsequent section.

### III. STATISTICS OF BOUNDARY LAYER UNDER THE TRIPPING EFFECT

#### A. Integral and global quantities

An overall assessment of the boundary layer under the tripping conditions is presented through the boundary-layer thickness. Figure 2(a) shows the distribution of  $\delta$  as a function of Reynolds number  $\text{Re}_\theta$  ( $\text{Re}_\theta = \theta U_\infty / \nu$ ,  $\theta$  is the momentum boundary layer thickness), across different trip-wire diameters and different free-stream velocities. The increasing  $\delta$  implies the deviation of velocity profiles from the canonical status. In Table I, the basic flow parameters manifest that the cases of L0, L1, M0, and H0 exhibit an undertripped state, consequently excluding them from further discussion within this paper.

To discern the degree of distortion of flow fields under the tripping influence, the distribution of the shape factor is considered the reference, which is given by  $H_{12} = \delta^* / \theta$  ( $\delta^*$  is the displacement thickness). Figure 2(b) shows that  $H_{12}$  is a function of  $\text{Re}_\theta$ . The values of  $H_{12}$  under all tripping conditions are also tabulated in Table I. The reference curve (in black line) proposed in Monkewitz *et al.* [26] is regarded as an indicator of the scatter in the current data under the influence of trips. It is worth noting that  $H_{12}$ 's for the cases with small  $D_c$  closely resemble the reference profile and then decrease and deviate from it with increasing  $\text{Re}_\theta$ . This trend indicates that the boundary layer is gradually overtripped in the adaptive region with increasing  $D_c$ . The overtripped effect leading to the decrease in  $H_{12}$  was also observed in the boundary-layer flows triggered by different tripping configurations [10,18], which is attributed to the alteration of the mean velocity scaling in the wake region. Coles' wake parameter  $\Pi$  was considered a measure of the wake strength [27]. Figure 2(c) shows the distribution of  $\Pi$  with respect to  $\text{Re}_\theta$ . The solid line is the wake parameter  $\Pi_{\text{num}}$  (the proposed threshold  $\Pi_{\text{num}} \pm 0.05$  in dashed lines) of the composite profile proposed in Chauhan *et al.* [28]. As shown,  $\Pi$  agrees with the proposed value for small  $D_c$  and then rapidly decreases and becomes negative as the wake region disappears in the strong tripping cases. The

TABLE I. Experimental parameters for the profiles of different tripping conditions at different free-stream speeds.

































Case	$D_t$ (mm)	Symbol	$U_\infty$ (m/s)	$Re_t$	$Re_{\delta^*}$	$Re_{\theta}$	$\delta$ (mm)	$\delta^*$ (mm)	$\theta$ (mm)	$v/u_\tau$ ( $\mu\text{m}$ )	$\Pi$	$H$	$l^+$	$\Delta t^+$	$TU_\infty/\delta$
L0	0	—	5.24	75	730	334	6.9	2.1	1.0	84.7	—	2.19	14.8	0.11	79 293
L1	1	—	5.40	81	759	333	6.9	2.1	1.0	82.1	—	2.18	15.2	0.11	83 173
L2	2		5.46	482	1398	947	29.6	3.9	2.7	59.5	0.30	1.43	21.0	0.21	19 356
L3	3		5.52	524	1503	1028	32.0	4.1	2.9	59.2	0.28	1.42	21.1	0.22	18 060
L4	4		5.50	525	1550	1062	32.3	4.3	3.0	59.7	0.29	1.41	20.9	0.21	17 838
L6	6		5.58	622	1702	1188	37.8	4.6	3.3	58.9	0.21	1.39	21.2	0.22	15 450
L8	8		5.49	796	1865	1335	48.8	5.2	3.8	59.4	0.03	1.35	21.0	0.22	11 797
L10	10		5.61	855	2079	1515	55.7	5.7	4.3	57.8	0.09	1.33	21.6	0.23	21 062
L12	12		5.67	1009	2177	1612	59.8	5.8	4.5	57.4	-0.08	1.31	21.8	0.23	19 843
L14	14		5.31	1208	2285	1714	76.3	6.5	5.1	61.2	-0.18	1.29	20.4	0.20	14 591
L17	17		5.35	1091	2147	1606	68.1	6.1	4.7	60.4	-0.15	1.30	20.7	0.21	16 457
L20	20		5.45	1237	2395	1803	76.3	6.7	5.2	59.8	-0.18	1.28	20.9	0.21	14 983
M0	0	—	8.90	151	844	431	6.9	1.5	0.8	41.2	—	1.96	31.3	0.19	54 214
M1	1		9.09	562	1586	1094	21.0	2.7	1.9	36.1	0.26	1.40	34.6	0.23	18 182
M2	2		8.95	688	2040	1412	27.0	3.5	2.5	38.1	0.34	1.40	32.8	0.21	13 886
M3	3		8.98	687	2134	1490	27.0	3.6	2.6	38.1	0.33	1.39	32.8	0.21	13 909
M4	4		8.98	757	2183	1542	29.6	3.7	2.7	37.8	0.26	1.37	33.1	0.21	12 713
M6	6		8.95	934	2416	1732	36.6	4.1	3.0	38.0	0.17	1.35	32.9	0.21	20 511
M8	8		8.91	1180	2643	1945	46.1	4.5	3.4	37.8	0.00	1.32	33.0	0.21	16 215

TABLE I. (Continued.)

Case	$D_e$ (mm)	Symbol	$U_\infty$ (m/s)	$Re_\tau$	$Re_\tau^*$	$Re_\theta$	$\delta$ (mm)	$\delta^*$ (mm)	$\theta$ (mm)	$v/u_\tau$ ( $\mu\text{m}$ )	$\Pi$	$H$	$I^+$	$\Delta I^+$	$TU_\infty/\delta$
M10	10		8.79	1462	2851	2140	56.9	4.9	3.8	37.7	-0.01	1.29	33.2	0.21	12964
M12	12		9.08	1693	3304	2514	65.3	5.5	4.3	37.4	-0.15	1.27	33.4	0.22	11652
M14	14		9.01	1753	3501	2691	68.1	5.9	4.7	37.6	-0.17	1.26	33.2	0.21	11094
M17	17		9.04	1907	3393	2606	73.6	5.7	4.5	37.4	-0.23	1.26	33.5	0.22	10311
M20	20		9.09	2253	3903	3032	87.3	6.5	5.2	37.5	-0.28	1.24	33.3	0.22	8739
H0	0	—	13.69	221	1060	606	6.8	1.2	0.7	27.5	—	1.75	45.5	0.21	85094
H1	1		13.66	916	2670	1952	24.3	3.1	2.2	25.7	0.32	1.37	47.2	0.22	23594
H2	2		13.49	898	2714	1976	24.3	3.2	2.3	26.2	0.36	1.37	46.3	0.21	23301
H3	3		13.54	1007	2842	2091	27.0	3.3	2.4	26.0	0.29	1.36	46.5	0.22	20989
H4	4		13.76	1121	2980	2213	29.6	3.4	2.5	25.6	0.24	1.35	47.3	0.23	19499
H6	6		13.65	1322	3265	2465	35.1	3.8	2.8	25.7	0.14	1.32	47.1	0.22	16321
H8	8		13.53	1833	3784	2952	48.8	4.4	3.4	25.8	-0.07	1.28	46.9	0.22	11619
H10	10		13.46	2342	4340	3460	62.6	5.1	4.0	25.9	-0.20	1.25	46.8	0.44	18044
H12	12		13.75	2674	5007	4023	70.8	5.7	4.6	25.6	-0.22	1.24	47.2	0.45	16283
H14	14		13.46	2821	5055	4077	76.3	5.9	4.8	26.2	-0.23	1.24	46.2	0.43	14794
H17	17		13.68	2786	4791	3871	73.6	5.5	4.4	25.6	-0.27	1.24	47.3	0.45	15595
H20	20		13.72	3546	5896	4813	95.0	6.7	5.5	25.9	-0.33	1.22	46.6	0.44	12106

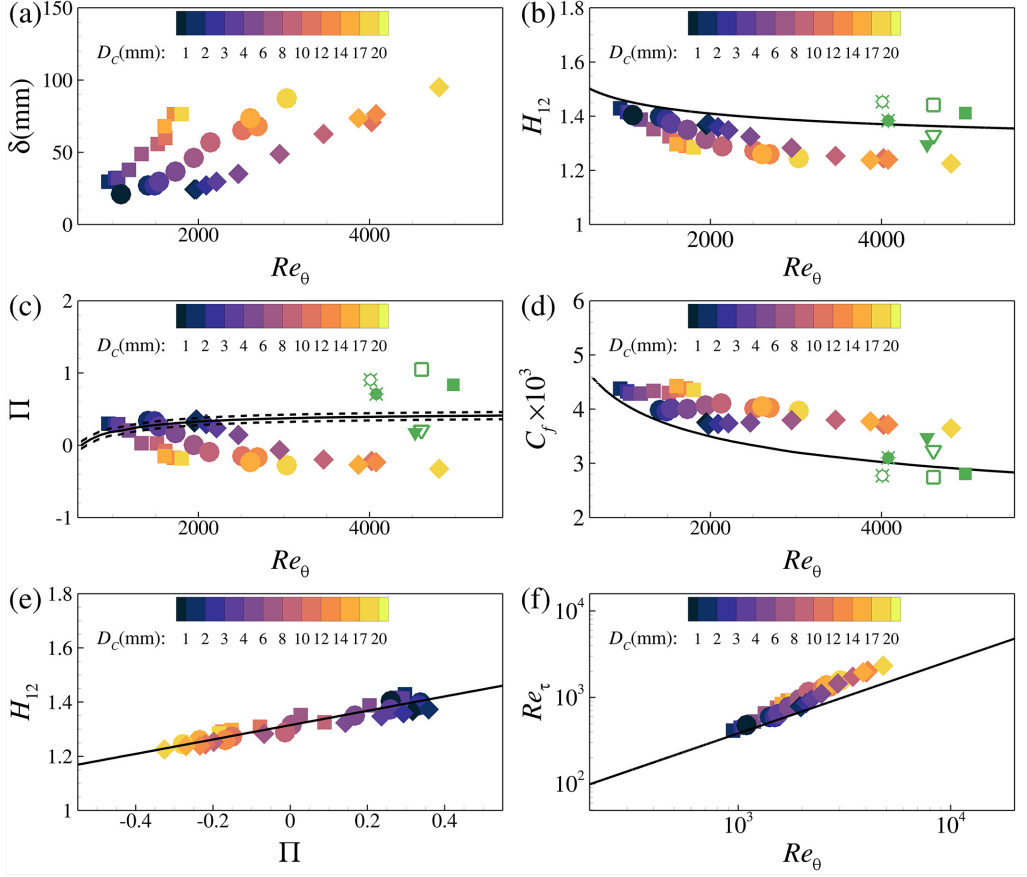


FIG. 2. (a) Boundary-layer thicknesses  $\delta$ , (b) shape factor  $H_{12}$ , (c) Coles' wake parameter  $\Pi$ , and (d) friction coefficient  $C_f$ , as a function of  $Re_\theta$  for various  $D_c$  and free-stream velocities. In subplot (b), the solid line represents the composite profile by Monkewitz *et al.* [26] as  $H_{12} = 1 + \frac{\kappa I_{WW}}{\ln(Re_\theta)} + \frac{\kappa^2 I_{WW} (I_{WW} - C)}{\ln^2(Re_\theta)} + \frac{\kappa^2 I_{WW} (\kappa I_{WW}^2 - I_{WW} - 2\kappa I_{WW} C + \kappa C^2)}{\ln^3(Re_\theta)}$ , with  $\kappa = 0.41$ ,  $I_{WW} = 7.11$ , and  $C = 3.3$ . In subplot (c), solid line:  $\Pi_{num}$  for the composite profile proposed in Chauhan *et al.* [28]; dashed line:  $\Pi_{num} \pm 0.05$ . In subplot (d), solid line: Coles-Fernholz skin-friction law  $C_f = 2(\kappa^{-1} \ln Re_\theta + C)^{-2}$ , with coefficient  $\kappa = 0.384$  and  $C = 4.127$  [29]. (e) The linear relation between  $H_{12}$  and  $\Pi$ . The solid line represents the fit to all data points, viz.  $H_{12} = 0.27\Pi + 1.31$ . (f) The relation between Reynolds numbers  $Re_\theta$  and  $Re_\tau$ . The solid line indicates the relation of  $Re_\tau = 1.13 \times Re_\theta^{0.843}$  by Schlatter and Örlü [13]. The data of the different tripping conditions in Rodríguez-López *et al.* [15] are involved for comparison: the two-rows-cylinder (*2row20*) case  $\nabla$ , the staggered-cylinder (*2stag20*) case  $\blacktriangledown$ , and the sawtooth (*Saw*) case  $\times$ . The empty and filled symbols denote the data at the streamwise locations of  $x = 1.3$  and  $1.6$  m, respectively.

decreased  $\Pi$  value was also reported by Marusic *et al.* [10] in the oversimulated boundary-layer flows under the tripping conditions of thread rods. In fact, by increasing  $D_c$  to be of the same order as or larger than the incoming boundary layer thickness, the tripping rod can induce a strong perturbation wake flow which has a predominant influence on the intermittency and mean profiles in the wake region [12, 13], consequently resulting in the significantly depleted wake parameter  $\Pi$ , as shown in Fig. 2(c). As another diagnostic alternative to assess the inner flow property under the tripping effects, the friction coefficient  $C_f$  against  $Re_\theta$  is plotted in Fig. 2(d). As shown,  $C_f$  is close to the Coles-Fernholz skin-friction law  $C_f = 2(\kappa^{-1} \ln Re_\theta + C)^{-2}$ , with coefficient  $\kappa = 0.384$  and



$C = 4.127$  [29] for the small  $D_c$ . With increasing  $D_c$ ,  $C_f$  remains nearly constant and deviates from the proposed curve. It has been documented that the estimation of  $C_f$  is dramatically affected by the trips in the adaptive region, the effect of which diminishes with an increase in the extent of the logarithmic layer [15]. This suggests that the relatively stable  $C_f$  observed at each free-stream velocity is attributed to the measurements taken far downstream, where the near-wall region and logarithmic layer should be recovered from the trip-wire effects.

Rodríguez-López *et al.* [15] conducted a comprehensive investigation into the mechanisms governing the formation of artificially generated TBL flows by designing the uniform and nonuniform wall normal distributions of blockage. They meticulously executed the one- and two-point hot-wire in the whole adaptive region, systematically observing the diagnostic quantities of  $H_{12}$ ,  $\Pi$ , and  $C_f$  to assess the recovery of the canonical properties. The data from the different trips located at  $x = 1.3$  and  $1.6$  m in their investigations are involved for comparison. The streamwise locations are comparable with our current experiment at  $x = 1.4$  m. The comparisons shown in Figs. 2(b)–2(d) reveal notable differences in the distribution of  $H_{12}$ ,  $\Pi$ , and  $C_f$  between the *Saw* case ( $\nabla$  and  $\blacktriangledown$ ) and the cylinder-family configurations [the *2row20* case ( $\odot$  and  $\bullet$ ) and the *2stag20* case ( $\square$  and  $\blacksquare$ )]. These parameters tend to cluster on opposing sides of the proposed curve within each subplot. The comparison indicates that, in contrast to the cylinder-family trip, the *Saw* trip exhibits similar properties to the current trip wire with large  $D_c$ . Both the *Saw* trip and the current trip wire demonstrate comparable distributions for both  $H_{12}$  and  $\Pi$ , derived from the mean velocity profiles. The relatively lower values of these parameters imply that the mean velocity profiles have a reduced wake [15]. Furthermore, this consistent deviation suggests that the boundary layers in the tripping conditions of the *Saw* trip and the current trip wire are generated by the wake-driven mechanism, likely attributed to the 100% blockage at the wall, as discussed in Rodríguez-López *et al.* [15].

To further observe the relation between  $\Pi$  and  $H_{12}$  across various trip-wire diameters at different free-stream velocities, all current datasets are employed to obtain a functional relation for  $\Pi$  in terms of  $H_{12}$ . Figure 2(e) illustrates the linear behavior of  $H_{12} = 0.27\Pi + 1.31$ , which provides a good fit. This suggests that either  $\Pi$  or  $H_{12}$  can serve as a diagnostic quantity to characterize the tripping impacts on the mean profile. Additionally, Fig. 2(f) presents the relationship between  $\text{Re}_\theta$  and  $\text{Re}_\tau$ . A functional relation of  $\text{Re}_\tau = 1.13 \times \text{Re}_\theta^{0.843}$  from Schlatter and Örlü [13] by compiling the canonical TBL data is included for comparison. As shown, under the current tripping effect, both  $\text{Re}_\tau$  and  $\text{Re}_\theta$  increase with enhancing  $D_c$ , and  $\text{Re}_\tau$  gradually deviates from the proposed relation curve. This deviation could also be associated with the modification of the mean profile in the wake region.

## B. Basic statistics and premultiplied spectra

Inner-normalized mean streamwise velocity and velocity-fluctuation variance profiles are shown in Fig. 3 for all the tripping conditions at varying free-stream velocities. At each free-stream speed, the mean velocity profiles ( $\langle U \rangle^+ \text{ vs } y^+$ ) for different  $D_c$  collapse in the near-wall region. For comparison, the inner velocity profile of Musker [30] is superimposed as a black line, in which von Kármán constant  $\kappa = 0.41$  and constant  $B = 4.86$  [31–33]. The results show that the mean profile in the inner region (loosely defined as  $y^+ \lesssim 100$ ) behaves canonically for all the trip wires, affirming the robustness of the law of the wall. The series of works by Rodríguez-López *et al.* [17,34] indicated that, in the region close to the tripping device, clear distortions of the mean profiles occur. Therefore, it can be inferred that the current measurement location is sufficiently far downstream, thereby avoiding direct impacts of the trip wires. The agreement also suggests that the near-wall region is more prone to adapting quickly to a canonical TBL, which is like that reported by Schlatter and Örlü [12]. On the other hand, there is an extension of the logarithmic region toward further positions with increasing  $D_c$ , which can be considered a proportional effect of the current trips. As shown, the upper bound of the log region extends up to approximately  $y^+ \approx 600$ . Considering that the upper bound of the log region in canonical TBLs is up to  $y^+ = 0.15\text{Re}_\tau$  [31], this observation implies that the boundary layer in the strong tripping condition has the potential to simulate and



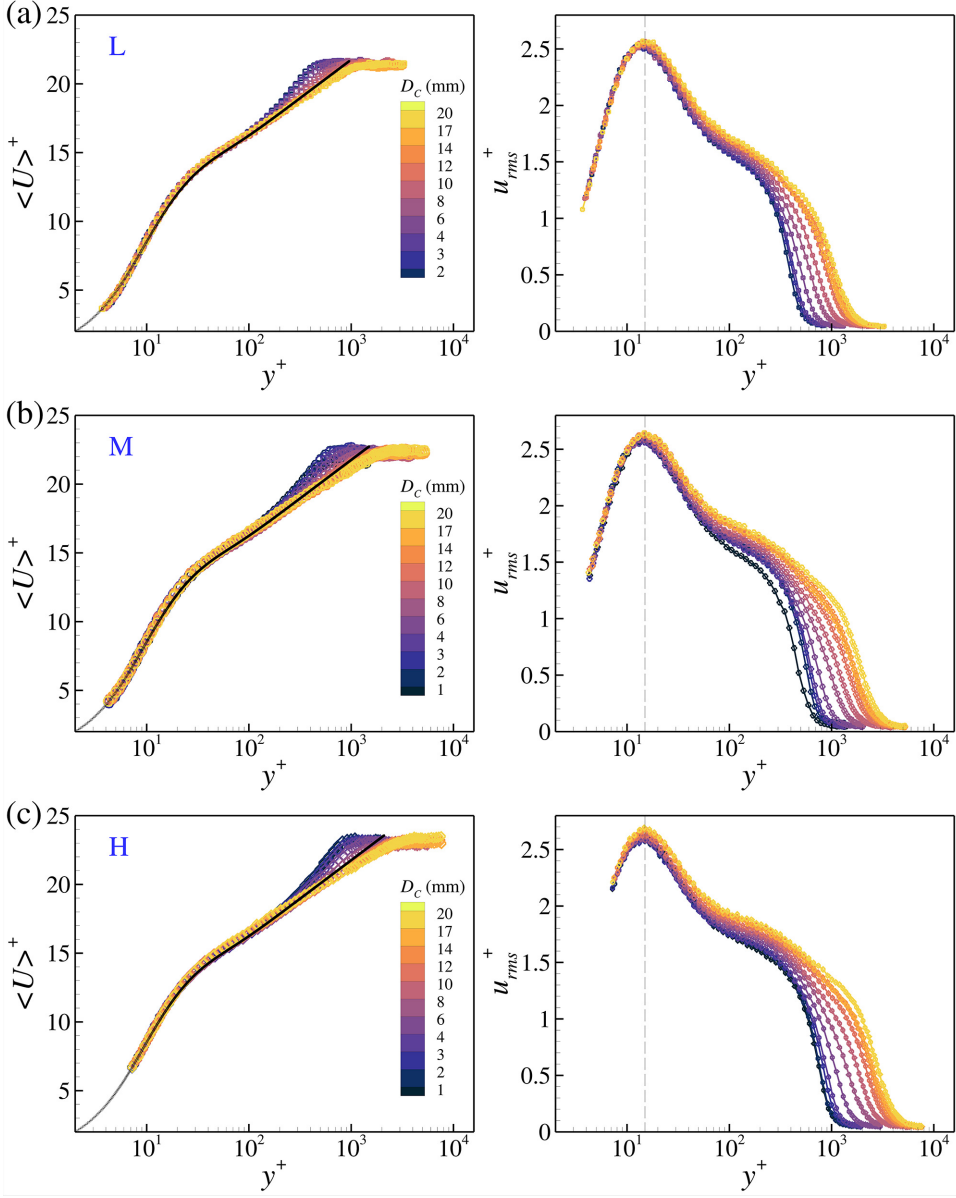


FIG. 3. Inner-normalized mean velocity profiles (left column) and streamwise velocity-fluctuation variance profiles (right column) for the different  $D_c$  at different free-stream speeds: (a) case L, (b) case M, and (c) case H. Left column: The solid black lines show the Musker profile [30] with constants  $\kappa = 0.41$  and  $B = 4.86$ . Right column: Dashed lines indicate the inner peak at  $y^+ \approx 15$ .

compare with a high- $\text{Re}_\tau$  TBL at  $\text{Re}_\tau \approx 4000$ . However, a significant difference is observed in the outer layer (in Fig. 3), presenting a progressively repressive wake region with increasing  $D_c$ , which is consistent with the decrease of  $\Pi$  [in Fig. 2(c)]. The systematic deviation in the wake region is consistent with the observations under different initial conditions, such as threaded tripping rods [10] and free-stream turbulence [35,36]. In canonical TBL flows, a velocity defect in the wake region is attributed to the large-scale intermittent mixing [27]. However, the current overtripped

effects could lead to a suppression of the wake region by introducing generated wake flows, which results in lower velocities in the modified region.

Accordingly, the inner-normalized root-mean-square (RMS) velocity fluctuation profiles  $u_{\text{rms}}^+(y^+)$  are shown in the right column in Fig. 3. The  $u_{\text{rms}}^+(y^+)$  profiles diverge in the outer region, which shows a systematic enhancement in the intensity level with increasing  $D_c$ . This enhancement in outer intensity is attributed to the turbulent wake flows introduced by the trip wires, which alter the structure of turbulence in the bulk of the boundary layer. The inner peak is consistently located at the wall-normal location of  $y^+ \approx 15$  for all the cases, as widely reported in canonical TBLs [3,37]. In this paper, the near-wall variance peaks are lower than the predicted value by Hutchins *et al.* [23], and the attenuation is no more than 6% for  $l^+ \leq 48$ . This attenuation should be attributed to the spatial-attenuation effect of hot-wire sensor length  $l^+$  and the low Reynolds number effect [22,23,37,38]. In fact, the spatial resolution of the hot-wire sensor could also have an attenuation impact on the higher frequency content of the turbulence energy, especially in the cases with decreasing viscous time scale [24]. For the main purpose of comparing different tripping effects, the attenuation effect of  $l^+$  on resolving the high-frequency content can be considered negligible in this paper. Although the difference between the inner peaks is relatively small, a closer examination reveals that the influence of the generated wake flows appears to be felt in the near-wall region, as evidenced by a certain growth in the inner peak with increasing  $D_c$ , especially at higher free-stream speeds. A possible explanation for the variation in inner-peak value is the growing superposition of larger-scale energy from wake structures in increasingly overtripped conditions.

Figure 4 shows premultiplied spectra of streamwise fluctuations  $k_x \phi_{uu}/u_\tau^2$  as a contour plot for each trip wire at the free-stream velocity in case H. The results of cases L and M are shown in the Appendix, which exhibit consistent results. The details of Fig. 4 are given in the figure caption. As shown, the similarity of  $k_x \phi_{uu}/u_\tau^2$  is noted near the wall, with the inner peak of the spectrogram located at  $y^+ \approx 15$  and a streamwise wavelength of  $\lambda^+ \approx 1000$ . The frequency domain is mapped to the wavelength domain by using the local mean velocity and Taylor's frozen field hypothesis. With increasing  $D_c$ , the premultiplied spectra in the outer region present the enhanced magnitude with the longer wavelength. In cases of small  $D_c$ , due to the insufficient scale separation at the relatively low  $\text{Re}_\tau$ , the outer spectral peak is barely distinguishable. Hutchins and Marusic [3] proposed that the scale separation begins to emerge for  $\text{Re}_\tau \gtrsim 2000$ , with the appearance of the outer energy site. This estimate is consistent with the current cases of  $D_c = 12\text{--}20$  mm ( $\text{Re}_\tau = 2674\text{--}3546$ ), showing the outer energy site. The emergence of the outer energy plateau is related to the enhancement of fluctuation variance shown in Fig. 3. It is deduced that the trip wire introduces large-scale energetic motions, which either originate from or are amplified by the shedding of the wake in the abruptly tripping conditions. As reported in the previous investigations in canonical TBL flows [5,8], an outer peak in the spectrogram emerges at  $y^+ \approx 3.9\text{Re}_\tau^{1/2}$  and  $\lambda_x/\delta \approx 6$ , corresponding to the very-large-scale motions. This location is marked by + in Fig. 4, which is used purely as a reference to compare with the current overstimulated cases. The mark + is approximately located at the position of the outer-energy plateau in the overtripped cases, which implies that the generated large scales have a comparable length scale as the very large-scale structures in the canonical high- $\text{Re}_\tau$  TBL flows. In this sense, increasing  $D_c$  can be viewed as a potential approach for simulating an increase in  $\text{Re}_\tau$  for TBL flows.

From the results of global quantities, mean velocity, and turbulent intensity profiles, it is indicated that the cases with a diameter of  $D_c = 2$  mm exhibit the canonical behavior at all the different free-stream velocities. The other cases are generally categorized as undertripped/overtripped. Thus, from a systematic perspective, the cases with the diameter of  $D_c = 2$  mm are selected as the reference ones for each free-stream velocity to observe differences in the premultiplied spectra. At the high free-stream velocity, the premultiplied spectrum in the case H2 is chosen to demonstrate differences  $\Delta k_x \phi_{uu}/u_\tau^2 = k_x \phi_{uu}/u_{\tau_{D_c=N}}^2 - k_x \phi_{uu}/u_{\tau_{D_c=2}}^2$ , where  $N = 1, 2, 3, 4, 6, 8, 10, 12, 14, 17$ , and 20. The composite spectrum of case H2 is regridded by cubic interpolation to match the range of the spectrum in other cases prior to the subtraction. For comparison, the boundary layer thickness  $\delta_{D_c}$  is chosen for dimensionless representation. As

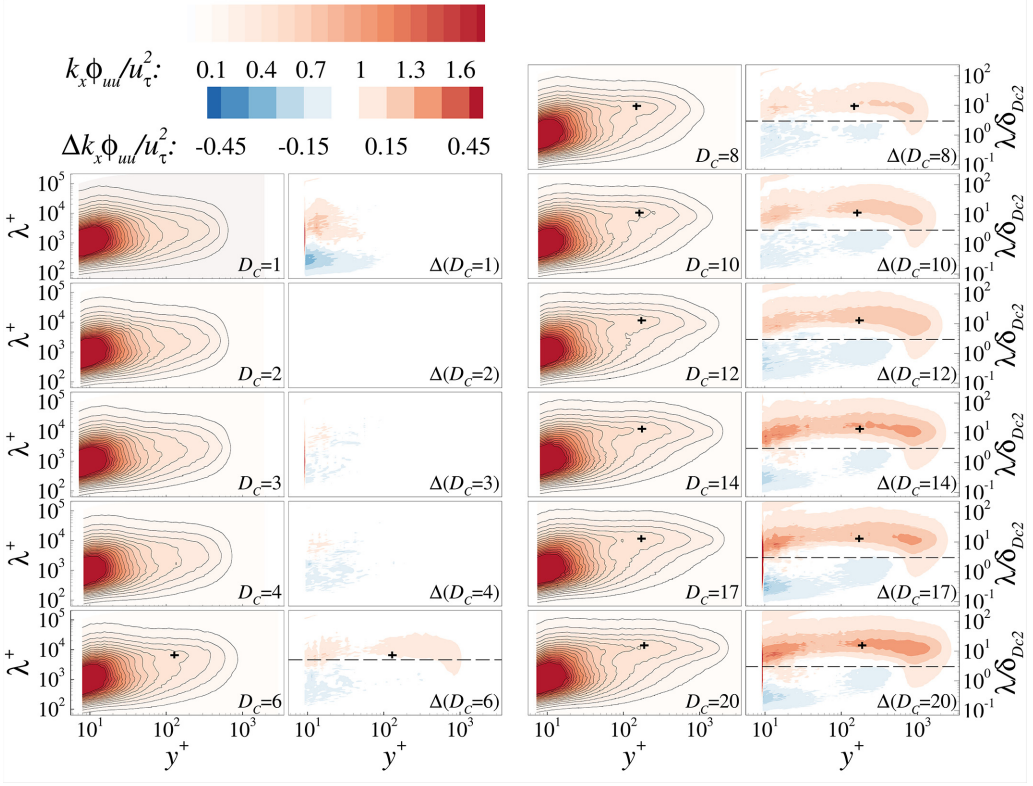


FIG. 4. Premultiplied velocity spectra of the fluctuation signal for various tripping diameters at the high free-stream velocity. Case  $D_c = 1$ –20 is labeled in each panel of the figure, correspondingly, in their right-hand panels, changes in spectrograms of all the tripping cases relative to case  $D_c = 2$  are shown, labeled as  $\Delta(D_c = 1$ –20) in each panel. The horizontal dashed line represents the wavelength of  $\lambda_x/\delta_{D_{c,2}} = 3$ . The boundary layer thickness of case H2  $\delta_{D_{c,2}}$  is chosen for normalization. The + symbol denotes the proposed outer peak of  $y^+ \approx 3.9\text{Re}_\tau^{1/2}$  and  $\lambda_x/\delta \approx 6$  [8].

expected, for the cases of small diameter ( $D_c = 3$  and 4 mm), the differences in energy content at any wavelength are quite small. For  $D_c = 1$  mm, there exists a certain discrepancy in the near-wall region, which validates the choice of case H2 as a reference to observe the spectra difference. It is evident that the tripping configurations with  $D_c > 6$  mm exhibit significant excess energy in the outer region. The increasing extent of excess energy with  $D_c$  implies that the physical dimensions of the trip wires directly influence the turbulence in the outer region. If we look carefully, the outer-layer excess energy is performed in a wide range of scales  $0.5 \lesssim \lambda_x/\delta_{D_{c,2}} \lesssim 200$  but predominantly concentrated near  $\lambda_x/\delta_{D_{c,2}} = 10$ –20 and  $y^+ \approx 800$ . Conversely, the region of reduced energy in the outer layer is noted in the vicinity of  $\lambda_x/\delta_{D_{c,2}} \approx 0.5$ –3 and  $y^+ \approx 100$ –300. It is suggested that the overtripped conditions introduce the large-scale motions that take over the outer layer and dominate the energy reassignment across multiscales. Additionally, the enhanced large-scale energy in the near-wall region seems to be the derivative of these energetic outer-layer large scales, with the extent of penetration dependent on the tripping intensity. This refers to the generated large scales penetrating down to the wall based on the footprint effect [3,6,7], which results in the increased near-wall peak in the broadband turbulence intensity (see Fig. 3). In summary, the current trip wires essentially simulate the effect of increasing the Reynolds number of TBL flows by introducing large-scale structures in the outer region.

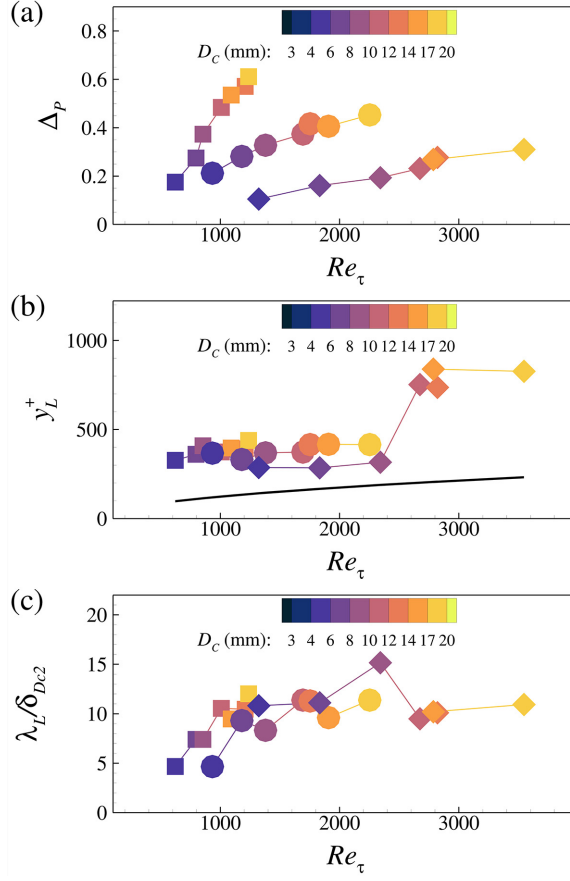


FIG. 5. Distribution of the discrepancy energy peak [(a)  $\Delta_P$ ], and the corresponding wall-normal height [(b)  $y_L^+$ ] and wavelength [(c)  $\lambda_L/\delta_{D_c2}$ ] against  $Re_\tau$  for all the tripping cases. The solid line in subplot (b) represents the relation of  $y^+ \approx 3.9Re_\tau^{1/2}$  proposed by Mathis *et al.* [8].

To further quantify the energy discrepancy, the proposed outer peak of  $y^+ \approx 3.9Re_\tau^{1/2}$  and  $\lambda_x/\delta \approx 6$  [5,8] is plotted in the discrepancy maps in Fig. 4. It is noted that the proposed peaks align with the region of increased energy, which means that the generated very large-scale structures have comparable length scales with the proposed ones. However, the symbols do not precisely match the discrepancy energy peak. This expected discrepancy suggests that the artificially generated large-scale structures in this paper cannot exactly replicate the canonical very large-scale motions (VLSMs). Figure 5 plots the distribution of the discrepancy energy peaks ( $\Delta_P$ ), along with their corresponding wall-normal heights ( $y_L^+$ ) and wavelength ( $\lambda_L/\delta_{D_c2}$ ) against  $Re_\tau$  for all tripping cases. As shown,  $\Delta_P$  increases as expected with  $D_c$  for each free-stream velocity. Interestingly, with increasing the free-stream speed, the extent of increase in  $\Delta_P$  is attenuated, which is likely attributed to the growth of the outer-layer turbulent intensity with increasing  $Re_\tau$  (free-stream velocity) in canonical conditions. The corresponding wall normal heights and wavelengths ( $y_L^+$  and  $\lambda_L/\delta_{D_c2}$ ) exhibit an overall increasing trend against  $Re_\tau$ . Notably, the wall normal height  $y_L^+$  is higher than the proposed value by Mathis *et al.* [8], which indicates that the occupation of the artificially generated large-scale structures predominantly resides in the wake region.

These statistical results clearly illustrate the alterations occurring in the outer region under the tripping effects. Rodríguez-López *et al.* [15] revealed that these outer-region alterations have an

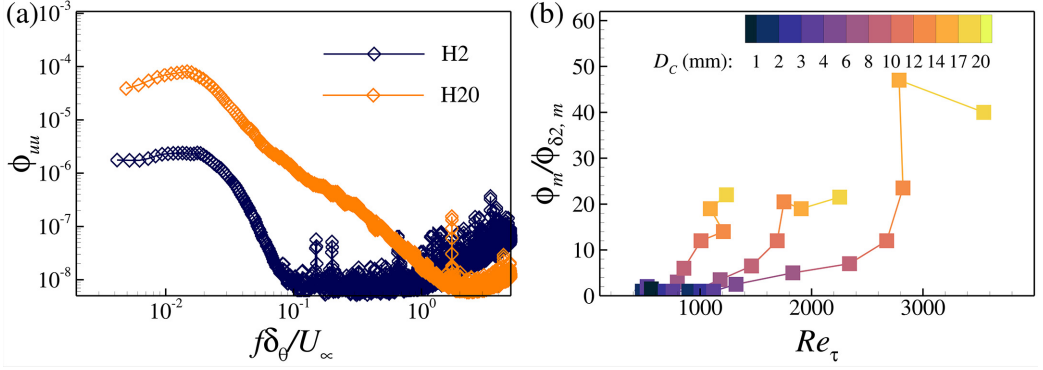


FIG. 6. (a) Power spectral density  $\phi_{uu}$  in the free-stream at  $y/\delta = 2$  for cases H2 and H20. (b) Distributions of power spectral density peaks normalized with that in the reference case  $\phi_m/\phi_{\delta_2, m}$  against  $Re_\tau$ .

influence on the free-stream (laminar) fluid above the boundary layer. Figure 6 shows the power spectral density  $\phi_{uu}$  at  $y/\delta = 2$  for the two representative cases of H2 and H20 (canonical and most overtripped cases). As suggested by Rodríguez-López *et al.* [15], the height of  $y/\delta = 2$  means that the hot-wire probe is sufficiently outside of the boundary layer, where the flow is permanently irrotational. In Fig. 6(a), it is evident that the case H20 presents significantly higher energy content with a low-frequency peak, attributed to the irrotational random motions of the potential flow outside of the turbulent-nonturbulent interface (TNTI) [15,39]. These irrotational events are accelerated/decelerated when the instantaneous TNTI is higher/lower than its average height, and their typical energy depends on the difference between the maximum and the minimum heights of the TNTI [15]. From this perspective, it can be inferred that the height difference of TNTI is larger in the overtripped cases, considering the stronger shedding wakes generated from the trip wires. To further explore the energy content with increasing tripping intensity, Fig. 6(b) plots the ratios of the power spectral density peak in the overtripped cases relative to that in the reference case  $\phi_m/\phi_{\delta_2, m}$ . Clearly, increasing  $Re_\tau$  enhances the peak intensity up to 20 times greater than the reference cases, meaning that the considerably intense fluctuations present in the wake of trip wires. Moreover, this result corroborates the argument that the height difference between the maximum and minimum of TNTI becomes larger and larger with increasing  $D_c$ .

### C. Higher-order moments and amplitude modulation

Figure 7 shows the distribution of high-order statistics in the form of the skewness  $S_u = \langle u^3 \rangle / \langle u^2 \rangle^{3/2}$  and the flatness  $F_u = \langle u^4 \rangle / \langle u^2 \rangle^2$ . As expected, clear scatters are noted for both  $S_u$  and  $F_u$  at the edge of the boundary layer. Despite this scatter, the overall trend remains consistent, characterized by negative  $S_u$  and positive  $F_u$ . This consistency underscores the persistence of the intermittent discontinuity between the free-stream and TBL (nonturbulence and turbulence) under the current tripping impacts.

On the contrary, both  $S_u$  and  $F_u$  approximately collapse in the inner region. At each free-stream velocity (cases L, M, and H), the tripping diameter  $D_c$  is considered the only parameter influencing the distribution, as other factors such as the free-stream velocity, hot-wire spatial length  $l^+$ , and viscosity length scale  $\nu/u_\tau$  are almost fixed (Table I). In Fig. 7, the near-wall  $S_u$  and  $F_u$  profiles demonstrate a remarkable collapse in each subplot, indicating the minimal influence of  $D_c$  on the near-wall distributions. Moreover, with increasing  $D_c$ , both  $S_u$  and  $F_u$  extend into the outer region, trying to preserve values typical of the logarithmic region. This could be the evidence to support the extension of the logarithmic region in the overtripped conditions.

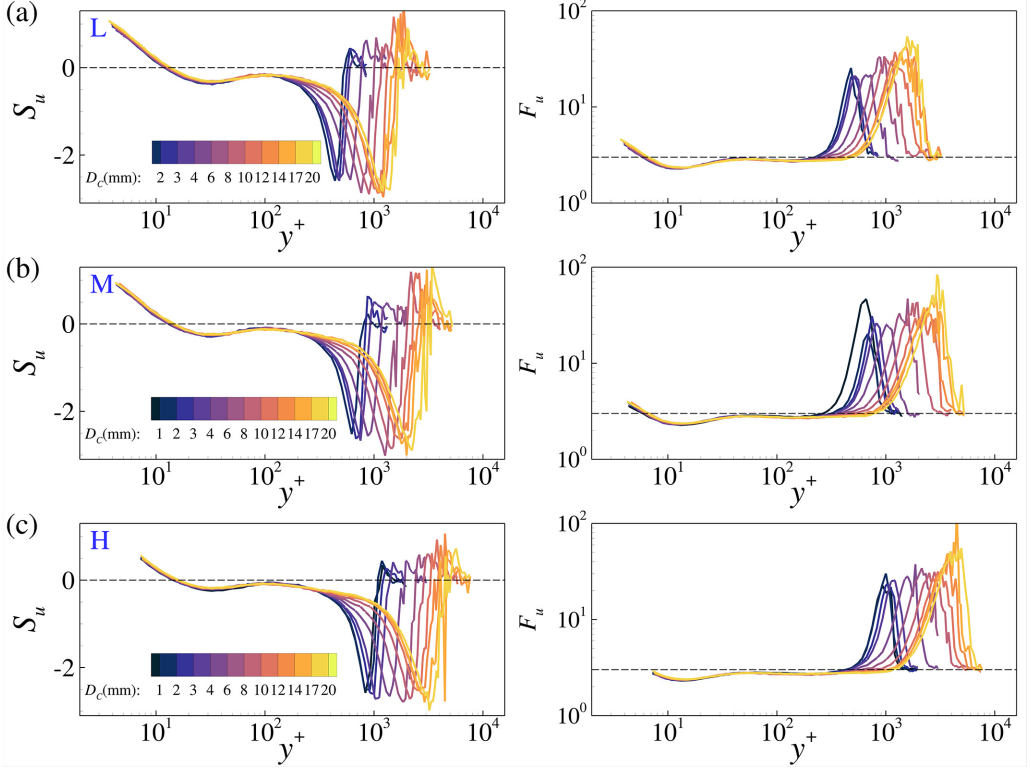


FIG. 7. Wall-normal profiles of the streamwise fluctuation skewness  $S_u$  (left column) and flatness  $F_u$  (right column) at different free-stream velocities: (a) case L, (b) case M, and (c) case H. Dash lines respectively represent  $S_u = 0$  and  $F_u = 3$ .

Figure 8 plots the negative peak value of the skewness ( $S_{u, \text{NP}}$ ) in the wall normal region of  $10 \lesssim y^+ \lesssim 100$  against the tripping diameter  $D_c$  normalized by  $\delta^*$  ( $D_c/\delta^*$ ). As shown, at each free-stream velocity,  $S_{u, \text{NP}}$  shows a slight increase with  $D_c/\delta^*$ . However, this growth is notably weaker than the influence caused by the free-stream velocity across all datasets. This observation indicates that the

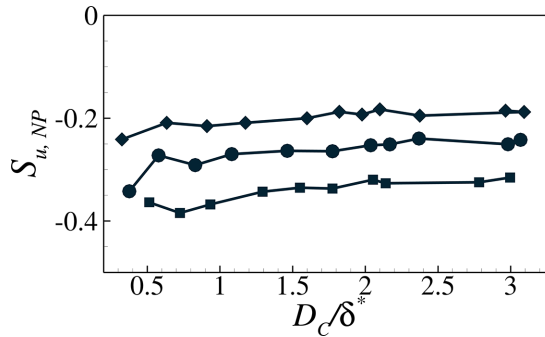


FIG. 8. Distribution of the negative peak value of the skewness  $S_{u, \text{NP}}$  against the normalized tripping diameter  $D_c/\delta^*$ . Square, circle, and diamond symbols represent the different free-stream velocities L, M, and H.



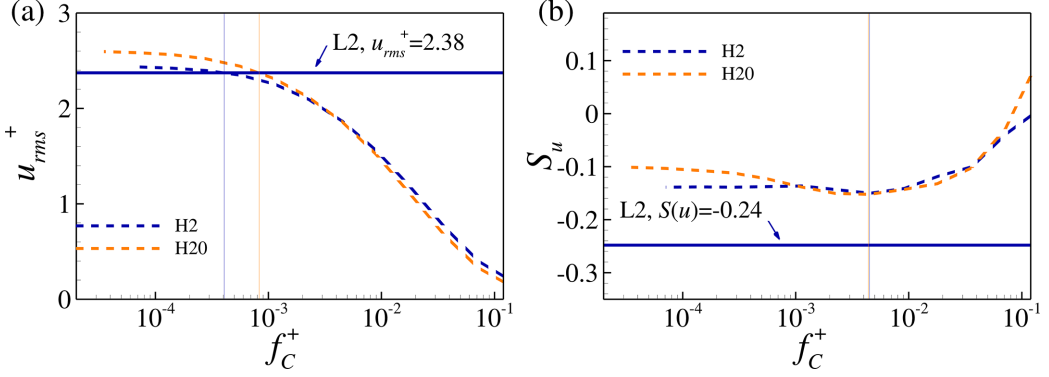


FIG. 9. Effect of applying a high-pass filter, with cutoff frequency  $f_C^+$ , to the streamwise velocity statistics (a)  $u_{rms}^+$ , (b)  $S_u$  of the cases H2 ( $Re_\tau = 898$ ) and H20 ( $Re_\tau = 3546$ ) at  $y^+ = 20$ . Solid horizontal lines represent the unfiltered result of case L2 ( $Re_\tau = 482$ ) at the corresponding wall normal location. Solid vertical lines denote the location at which the filtered data of H2 and H20, respectively, reach the unfiltered values of  $u_{rms}^+$  in case L2 and get their minimum values of  $S_u$ .

free-stream velocity should be the more dominant parameter influencing the skewness distribution, overshadowing the impact of the tripping diameter.

The skewness factor  $S_u$  in Fig. 7 exhibits a negative peak in the region of  $20 \lesssim y^+ \lesssim 30$ , which is consistent with the low Reynolds number results by Metzger and Klewicki [40]. They found that  $S_u$  exhibits the discrepancy in the near-wall region for a wide range of Reynolds numbers and revealed that the disparities originate mostly from the large-scale motions which have a direct interaction with the small scales. Considering the artificially generated large scales in this paper, we apply a high-pass filtering procedure to the field data at  $y^+ = 20$  as processed by Metzger and Klewicki [40]. This position of  $y^+ = 20$  corresponds closely to the negative peak observed in  $S_u$  and the peak of  $u_{rms}^+$ . We examine three representative Reynolds number cases for observation: (1) case L2 ( $Re_\tau = 482$ ), the canonical case at low free-stream velocity, which serves as the reference case; (2) case H2 ( $Re_\tau = 898$ ), the canonical case at high free-stream velocity; and (3) case H20 ( $Re_\tau = 3546$ ), the most overtripped case at high free-stream velocity. Figure 9 illustrates the effect of high-pass filter on  $u_{rms}^+$  and  $S_u$  for cases H2 and H20 against the inner normalized cutoff frequency  $f_C^+$  ( $f_C^+ = f\nu/u_\tau^2$ ). Solid horizontal lines represent the unfiltered case L2 at the corresponding wall normal location. The filtered  $u_{rms}^+$  values for cases H2 and H20 converge to the unfiltered result of case L2 at the cutoff frequencies of  $f_C^+ = 0.0004$  and  $0.0008$ , as marked by the solid vertical lines. In Fig. 9(b), both cases H2 and H20 obtain the minimum  $S_u$  near a sufficiently large cutoff frequency of  $f_C^+ \approx 0.0045$ . It is noted that the  $S_u$  minimum is still higher than the unfiltered case L2 value, which is possibly due to the relatively narrow range of  $Re_\tau$ . The systematical elimination of any additive effect of large-scale, low-frequency motions on the measured statistics by high-pass filtering procedure suggests that the observed differences in  $f_C^+$  between the low-speed case (L2) and the high-speed cases (H2 and H20) stem from the increasing range of large scales inherent in the high-speed flow and introduced by the tripping conditions. Through high-pass filtering, the disparities of the cutoff frequency suggest the existence of some direct coupling, albeit weak, between the large and small scales of motion [40]. Furthermore, the filtered  $u_{rms}^+$  values approach the case L2 values at a higher cutoff frequency in case H20 than case H2. This implies that the artificially generated large scales could further enhance the energy of the small scales by more direct interactions.

Given the emergence of large-scale structures in the outer layer in the current tripping conditions, it becomes imperative to examine the modulation effect of these large scales on small-scale structures. To achieve this, a filter with a cutoff wavelength of  $\lambda_x/\delta_{D_{c2}} = 3$  (the horizontal dashed



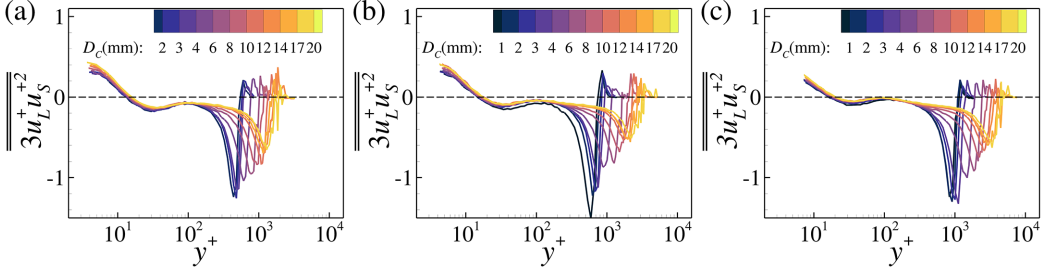


FIG. 10. Wall-normal profiles of  $\overline{3u_L^+ u_S^{+2}}$  at the different tripping conditions with different free-stream velocities: (a) case L, (b) case M, and (c) case H.

line in Fig. 4) is chosen as a reasonable demarcation to separate the fluctuating velocity signal into the large and small scales ( $u_L$  and  $u_S$ ). Although the choice of cutoff length may introduce some bias in  $\overline{3u_L^+ u_S^{+2}}$  at a given Reynolds number (or a certain flow condition), we assume that the current choice of cutoff wavelength has no considerable effect on the scale interactions, which are intended to emphasize the various trip-wire effects.

It has been accepted that the amplitude modulation (AM) effect of large scales can be evaluated from skewness analysis [35, 41–43]. The profile of the cross-term of the scale-decomposed skewness factor  $\overline{3u_L^+ u_S^{+2}}$  closely resembles to the AM coefficient between the large scales and the envelope of small scales [8, 41]. Thus, we utilized the cross-term of the scale-decomposed skewness factor to diagnose the AM effects under the tripping impacts. By using a scale-decomposed signal  $u^+ = u_L^+ + u_S^+$ , the skewness factor  $S_u$  can be expressed in the form:

$$S_u = \overline{u_L^{+3}} + \overline{3u_L^+ u_S^{+2}} + \overline{3u_L^+ u_S^{+2}} + \overline{u_S^{+3}}, \quad (1)$$

with  $\overline{\bar{X}} = \bar{X}/(\overline{u^{+2}})^{3/2}$ , where a single overbar indicates the time average. Figure 10 shows the distribution of the cross-term  $\overline{3u_L^+ u_S^{+2}}$ . Like the distribution of  $S_u$  in Fig. 7,  $\overline{3u_L^+ u_S^{+2}}$  exhibits agreement in the inner region and discrepancy in the outer region. Looking carefully,  $\overline{3u_L^+ u_S^{+2}}$  shows a slight growth in the near-wall region with increasing  $D_c$ . Even though the current Reynolds number is relatively lower, this subtle growth in  $\overline{3u_L^+ u_S^{+2}}$  reveals that the large scales have an enhanced AM effect on the near-wall small scales with increasing the tripping intensity. On the other hand, it was argued that the AM effect can be interpreted as a phase relationship between the large and small scales [44]. The distribution of  $\overline{3u_L^+ u_S^{+2}}$  suggests that the phase relationship is unchanged under the tripping impact, which remains in phase ( $\overline{3u_L^+ u_S^{+2}} > 0$ ) approximately below the buffer layer and exhibits the critical layer behavior ( $\overline{3u_L^+ u_S^{+2}} \approx 0$ ) in the log layer. The negative  $\overline{3u_L^+ u_S^{+2}}$  in the outer region is interpreted as a reversed scale arrangement phenomenon, which is the consequence of the outer-layer intermittency. Under tripping impacts,  $\overline{3u_L^+ u_S^{+2}}$  holds the attenuated values in the outer region, which means that the intermittency is somewhat modified due to the wake flow generated from the trip wires.

In Fig. 11, we compare the wall-normal profiles of  $\overline{3u_L^+ u_S^{+2}}$  at three Reynolds numbers (L2:  $\text{Re}_\tau = 482$ , H2:  $\text{Re}_\tau = 898$ , and H20:  $\text{Re}_\tau = 3546$ ) to observe the effect of tripping diameter and free-stream velocity on the scale interactions. It is evident that the near-wall  $\overline{3u_L^+ u_S^{+2}}$  has higher values in cases H2 and H20 (especially in the negative-peak region of  $20 \lesssim y^+ \lesssim 30$ ), which indicates that the free-stream velocity enhances the AM effects. Moreover, the value of case H20 is even higher than that of case H2 (almost increased 40% in the near-wall region), suggesting that

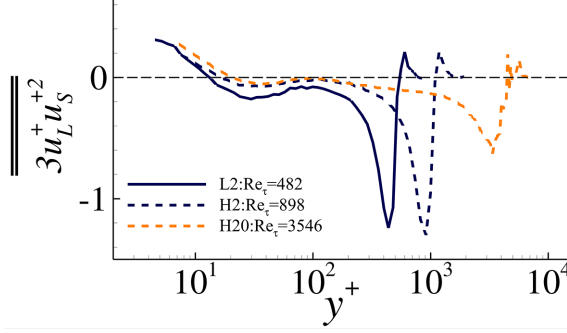


FIG. 11. Wall-normal profiles of  $\overline{3u_L^+ u_S^{+2}}$  at the three cases. L2:  $\text{Re}_\tau = 482$ , H2:  $\text{Re}_\tau = 898$ , and H20:  $\text{Re}_\tau = 3546$ .

the tripping diameter also influences the AM results. Thus, it can be inferred that both the tripping diameter and the free-stream velocity are the influence parameters affecting scale interactions in the current experiments.

Moreover, to further explore the nature of the scale interactions at an equivalent  $\text{Re}_\tau$  as discussed in Rodríguez-López [15], Fig. 12 compares  $\overline{3u_L^+ u_S^{+2}}$  at two nominally matched Reynolds numbers:  $\text{Re}_\tau \approx 1200$  ( $\text{Re}_\tau \approx 1237$  at case L20,  $\text{Re}_\tau \approx 1180$  at case M8, and  $\text{Re}_\tau \approx 1322$  at case H6) and  $\text{Re}_\tau \approx 2300$  ( $\text{Re}_\tau \approx 2253$  at case M20 and  $\text{Re}_\tau \approx 2342$  at case H10). Note that the comparisons are not for perfectly matched values of  $\text{Re}_\tau$ . As shown in Fig. 12, obvious differences are observed in the wake region, suggesting the persistence of remnants from the trip wires at the measurement location. That is, the artificially generated large-scale structures predominantly modify the outer intermittency to varying degrees. This result is consistent with that reported by Rodríguez-López *et al.* [15]. Closer observation of the profiles in the inner region reveals that the  $\overline{3u_L^+ u_S^{+2}}$  profiles do not exhibit a perfect collapse. This observation suggests that, while the AM intensity and the phase relationship between the large and small scales generally follow a consistent distribution trend, they still display some degree of discrepancy at the nominal equivalent  $\text{Re}_\tau$ .

#### IV. FM

The emergence of large-scale structures in the outer layer with increasing tripping intensity raises our interest in the scale interaction of the overtripped boundary layer. Apart from the

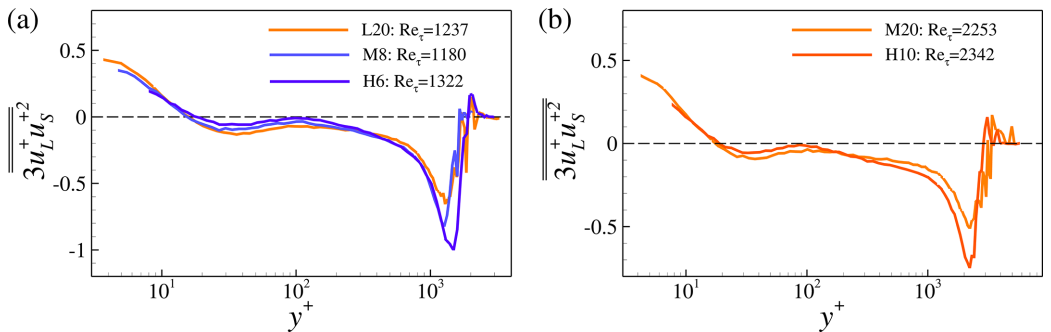


FIG. 12. Comparisons of  $\overline{3u_L^+ u_S^{+2}}$  at two nominally matched Reynolds numbers: (a)  $\text{Re}_\tau \approx 1200$  (L20:  $\text{Re}_\tau = 1237$ , M8:  $\text{Re}_\tau = 1180$ , and H6:  $\text{Re}_\tau = 1322$ ) and (b)  $\text{Re}_\tau \approx 2300$  (M20:  $\text{Re}_\tau = 2253$  and H10:  $\text{Re}_\tau = 2342$ ).

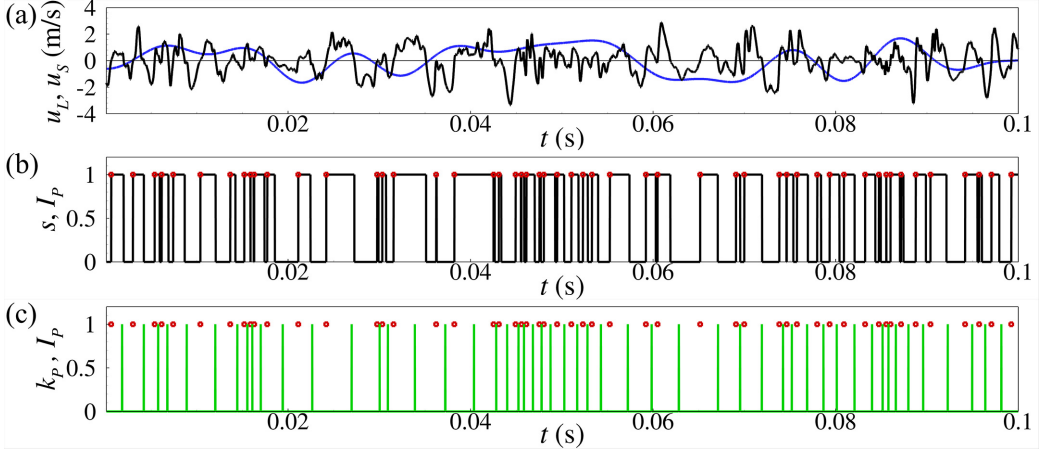


FIG. 13. (a) An interval of large- and small-scale components ( $u_L$  and  $u_s$ , blue and black lines), extracted from the fluctuation signal at  $y^+ \approx 15$  for case H2. (b) The TA  $s(t_i)$  is shown in a black line, and the instants for upcrossing of zero are marked by red squares. (c) The frequency indicator function  $k_P$  is shown in the green pulse, and  $I_P$  is also plotted for reference.

well-documented AM phenomenon, FM has received relatively less attention to date, primarily owing to the difficulty of robustly quantifying the instantaneous frequency of small scales in broadband signals [6,7,45–48]. The observation of scale interactions has demonstrated that the small scales, characterized by high frequency, are related to the regions of intense vorticity, which have a characteristic length of the local Taylor microscale [6,49,50]. It has been reported that the zero-crossing interval is related to Taylor’s microscale, fine structures, and vorticity distribution [51]. Therefore, the derivative of zero crossings is developed to quantify the instantaneous frequency for the observation of the FM effect.

Figure 13 shows a schematic representation of the procedure proposed to isolate the modulation effects of large scales on the small-scale frequency, and the procedure is as follows:

- (i) The decomposed large-scale ( $u_L$ ) and small-scale ( $u_s$ ) fluctuations are acquired by a spectral filter of length  $\lambda_x/\delta_{D_{c2}} = 3$ , which is also used for the discussion of AM effects in Figs. 10–12.
- (ii) The telegraph approximation (TA) of small scales is obtained  $s(t_i)$ , as shown in the black line. Then the instants exhibiting up crossings of zero  $I_P(t_i)$  are extracted and marked by red squares. It is worth noting that the zero crossing with up or down crossings provides consistent results. The interval between every two successive  $I_P(t_i)$  is interpreted as a measure of the instantaneous period, by analogy with the concept of instantaneous frequency [52].
- (iii) To quantify the representative instantaneous frequency, the center of every two successive  $I_P(t_i)$  is defined as an indicator function  $k_P(t_i)$  of the instantaneous frequency, expressed as

$$k_P[t_{(n+m)/2}] = \begin{cases} 1 & \text{if } I_P(t_n) = 1 \quad \text{and} \quad I_P(t_m) = 1, \quad (m = \min\{n+1, \dots, N\}) \\ 0 & \text{otherwise.} \end{cases} \quad (2)$$

It is evident that the indicator function,  $k_P(t_i) = 1$ , refers to the instants which can be used to count for calculating the small-scale frequency, based on the idea that the local frequency is proportional to the amounts of  $k_P(t_i) = 1$  per unit length of the series. For a given signal length, the higher the amount of  $k_P(t_i) = 1$  per unit length, the higher the representative frequency of the signal, and vice versa. The above procedure shows that the frequency indicator is derived strictly following the zero-crossing events without setting any thresholds.

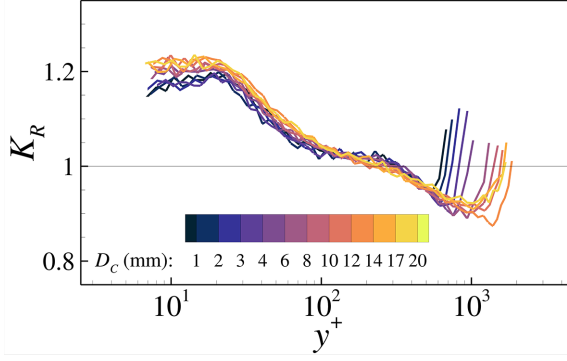


FIG. 14. The ratio of large-scale conditional averaging zero-crossing frequency  $K_R$ , as a function of the wall-normal coordinate  $y^+$ , in boundary layers for various tripping diameters for case H.

Then we introduce the ratio  $K_R$  to quantify FM, defined as

$$K_R = \frac{\sum_{i=1}^N [k_P(t_i) s_{u_L}(t_i)] / \sum_{i=1}^N [s_{u_L}(t_i)]}{\sum_{i=1}^N \{k_P(t_i)[1 - s_{u_L}(t_i)]\} / \sum_{i=1}^N [1 - s_{u_L}(t_i)]}, \quad (3)$$

where  $s_{u_L}(t_i)$  is a TA of large-scale structures  $u_L(t_i)$  as

$$s_{u_L}(t_i) = \frac{1}{2} \left[ \frac{u_L(t_i)}{|u_L(t_i)|} + 1 \right]. \quad (4)$$

The value of  $K_R > 1$  signifies that the frequency is statistically higher during the intervals of  $u_L > 0$  than during  $u_L < 0$ , indicating a positive FM effect. This means that an increase of the local frequency in small scales becomes aligned with  $u_L > 0$  and a decrease for  $u_L < 0$ . In addition, the negative FM effect can be characterized by  $K_R < 1$ , and the absence of FM is given by  $K_R \approx 1$ .

The values of the ratio  $K_R$  as a function of the wall-normal coordinate  $y^+$  are shown in Fig. 14 for the cases at high-speed free-stream velocity. In the plot, the values of  $K_R > 1$  appear in the near-wall region, while moving away from the wall,  $K_R$  becomes  $< 1$ , which indicates a reversal in the FM effects. The overall behaviors are in accordance with previous investigations on FM in canonical wall-bounded turbulence [6,45–48]. However, the behavior of  $K_R$  also highlights the specific features that depend on the tripping conditions with different  $D_c$ . The degree of FM close to the wall is enhanced by increasing  $D_c$  ( $\sim 40\%$  if we set  $K_R = 1$  as the datum point to differentiate the positive and negative FM), which indicates that the generated large-scale structures enhance the near-wall FM process in the overtripped cases, like the consequence of increasing  $Re_\tau$  in canonical TBL flows. This distribution of  $K_R$  could be related to the distortion of near-wall structures below the buffer layer caused by the strong sweeps (splatting) of large scales [53]. As increasing  $D_c$  and the free-stream velocities, the higher  $K_R$  values in the range of  $y^+ \lesssim 20$  suggest that the generated large-scale structures promote the transportation of the high-intensity small scales toward the wall, which causes a stronger distortion of the small scales through the splatting mechanism. On the other hand, away from the wall, the reversal mechanism of FM is noted in a V-like shape of  $K_R$  in the outer region, which is strengthened with increasing  $D_c$ . The scale arrangements in the outer region are the consequence of the intermittent exposure of the hot wire to an alternating occurrence of turbulent/nonturbulent fluids. Under the tripping effect, the range of the V-like shape of  $K_R$  expands with increasing the boundary layer thickness, confirming the above conclusion that the trips significantly modify the outer region while preserving intermittency.

Like the discussion of  $3u_L^+ u_S^{+2}$  in Fig. 12, Fig. 15 shows the comparisons of  $K_R$  at nominally matched Reynolds numbers to examine the nature of the FM effects. The FM profiles show an acceptable agreement in the inner region, as indicated by the relatively dispersed distribution of

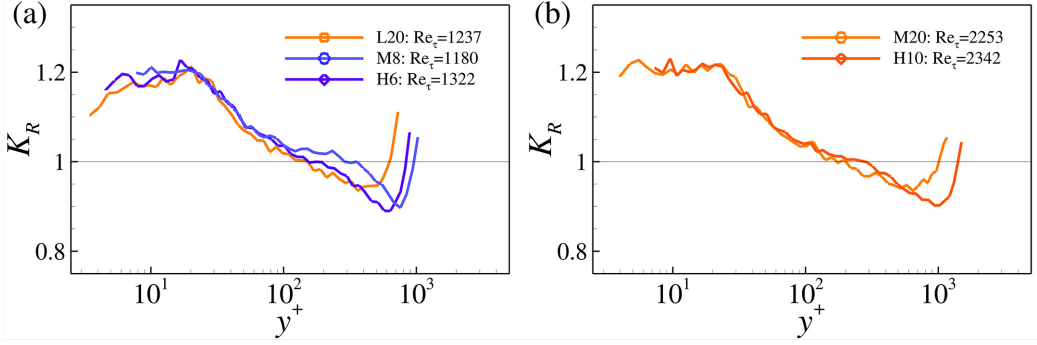


FIG. 15. Comparisons of  $K_R$  at two nominally matched Reynolds numbers (the same as in Fig. 12).

$K_R$ . As anticipated, a noticeable discrepancy appears in the wake region associated with the trip-wire effects. These results support the proposal that attention should be paid when comparing scale interactions (both AM and FM) at matched Reynolds numbers if the boundary layers have not fully recovered from specific tripping conditions. Furthermore, it evokes our attention to the behavior of the intermittency in the outer region under the impacts of trip wires, which will be discussed in the following section.

## V. INTERMITTENCY IN THE OUTER REGION

According to Corrsin and Kistler [54], the outer-layer intermittency is described as the flow alternating between turbulent and substantially irrotational nonturbulent motions. To observe the intermittency behavior, it is necessary to detect the TNTI. Various threshold-detecting methods have been developed, based on vorticity [55] and enstrophy [56] in numerical simulation datasets. For the experimental data of relatively high level of free-stream turbulence, the TNTI was detected by the technique based on turbulent kinetic energy [57], local homogeneity [58], fuzzy clustering of the velocity field [59], track of the Lagrangian particle trajectories [60], and so on. For one-dimensional flow data by hot-wire measurement, the detection relies upon identifying whether the probe is measuring turbulent or nonturbulent fluids. Therefore, a turbulent kinematic energy (TKE) criterion proposed by Chauhan *et al.* [57] is utilized for the current hot-wire data. This procedure has been extensively used in many previous works for the detection of TNTI [16,57,61–63], and a brief description is given here. The TNTI detector function is expressed as

$$\hat{k}(i) = \frac{100}{U_\infty^2} \frac{1}{3} \sum_{j=-1}^1 (U_{i+j} - U_\infty)^2, \quad (5)$$

where the index  $i$  is an arbitrary instant in the temporal domain, and summation over index  $j$  indicates a mean over three consecutive measurements in a time series. The turbulent (nonturbulent) fluids can be detected based on whether  $\hat{k}(i)$  is higher (lower) than a given threshold  $k_{th}$ . Utilizing this threshold, a binary representation of the flow is obtained, defined as

$$\hat{k}_b(i) = \begin{cases} 1, & \hat{k}(i) \geq k_{th} \\ 0, & \hat{k}(i) < k_{th}. \end{cases} \quad (6)$$

Then as proposed by Klebanoff [64], an intermittency parameter  $\gamma(y)$  at the wall-normal location of  $y$  is defined as

$$\gamma(y) = \frac{1}{N} \sum_{i=1}^N \hat{k}_b(i, y), \quad (7)$$

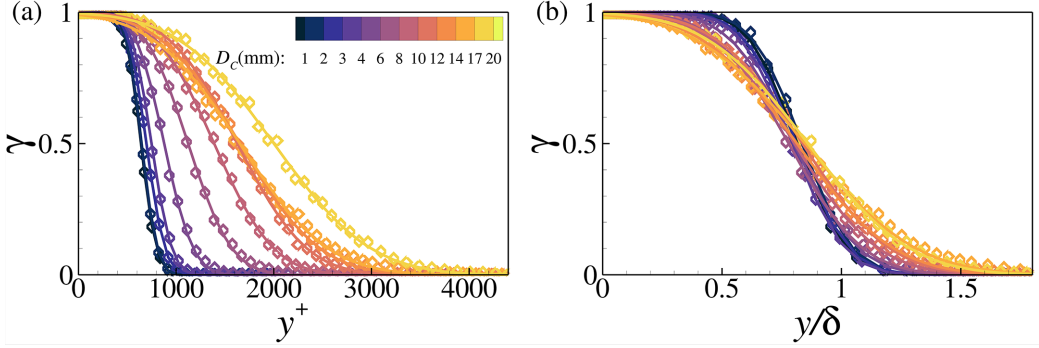


FIG. 16. Wall-normal intermittency profile  $\gamma(y)$  in inner and outer scaling (left and right column) for various  $D_C$  for case H. Color lines represent the result by fitting  $\gamma(y)$  to the error function.

which reflects the proportion of time that the flow is turbulent. Close to the wall, the flow is expected to be fully turbulent,  $\gamma(y) = 1$ , the nonturbulent fluids gradually have more occurrence far away from the wall, and  $\gamma(y) = 0$  in the free stream. It is well known that the intermittency profile  $\gamma(y)$  in a canonical TBL is described by the error function [54,64,65]:

$$\gamma(y) = \frac{1}{\sigma_I \sqrt{2\pi}} \int_y^\infty \exp\left[-\frac{(y - Y_I)^2}{2\sigma_I^2}\right] dy. \quad (8)$$

Here,  $Y_I$  is the wall-normal location of the mean interface, where  $\gamma(Y_I) = 0.5$  and  $\sigma_I$  is the standard deviation of instantaneous interface position  $y_I$  relative to the mean position  $Y_I$ . Both  $Y_I$  and  $\sigma_I$  are estimated parameters obtained by fitting the measurement intermittency profile to the function of Eq. (8). From the above definition, it is evident that the intermittency  $\gamma(y)$  is dependent on the given threshold value  $k_{th}$ . Based on the known free-stream intensity in this paper, a threshold of  $k_{th} \approx 0.07$ – $0.08$  is chosen to calculate  $\gamma(y)$ .

Figure 16 plots the  $\gamma(y)$  profiles against the normalized wall-normal distance in inner and outer scaling ( $y^+$  and  $y/\delta$ ) for the tripping cases at high free-stream velocity. Here,  $\gamma(y)$  exhibits a normal distribution with the mean interface location at  $Y_I/\delta \approx 0.81$ – $0.82$  and standard deviation  $\sigma_I/\delta \approx 0.15$ – $0.18$  at cases L2, M2, and H2, consistent with the previous investigations in canonical TBL flows [54,65]. The agreement affirms the availability of the TKE-based TNTI detecting approach and the corresponding threshold  $k_{th}$ . The inner scaling results in the left column in Fig. 16 show that, with increasing boundary-layer thickness  $\delta^+$  (with increasing  $D_C$ ), the intermittency region extends far away from the wall. On the other hand, the outer scaling results (right column) indicate that the intermittent region exhibits a wider proportion in the boundary layer, as evidenced by the increasing value of  $\sigma_I$ . Here,  $\sigma_I$  is a suitable measure of the width of the intermittent zone and is also deemed as an indicator parameter of the wrinkle amplitude of TNTI. Due to the enhanced wake shedding in the outer region from the trips, it is reasonable to have the large tortuosity of TNTI and the correspondingly thickened intermittent zone.

To further characterize the feature of the (ir)regularity of TNTI, Fig. 17 shows probability density functions (PDFs) of the length of the turbulent and nonturbulent segments ( $l$ ). The time interval that the continuous turbulent or nonturbulent fluids between every two adjacent TNTI points is converted into segment length  $l$  by using Taylor's frozen hypothesis. Figure 17 plots the PDF of  $l$  at different wall-normal heights (corresponding to  $\gamma = 0.1$ – $0.9$ ) for all the tripping cases. It is easy to accept that longer turbulent segments are prevalent in the region close to the wall ( $\gamma \rightarrow 0.9$ ), and the nonturbulent segments have a broader length scale toward the boundary layer edge ( $\gamma \rightarrow 0.1$ ). Both situations lead to long segments  $l$ . For  $\gamma \approx 0.5$ ,  $l$  has a relatively narrower distribution range, as turbulent and nonturbulent regimes appear in the equivalent scale with relatively shorter  $l$ . More

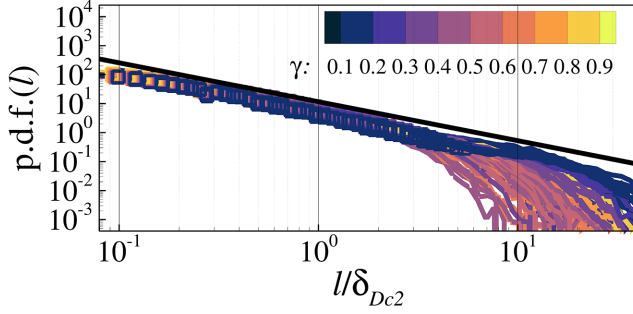


FIG. 17. Distribution of PDF( $l$ ) at the wall-normal heights in the range of  $0.1 \leq \gamma(y) \leq 0.9$ , under all the tripping effects for case H. The solid black line indicates an exponential distribution with a power-law scaling exponent of  $\zeta \approx -\frac{4}{3}$ . The square symbols represent the intermediate range between  $\lambda_T$  and  $l_{\text{mean}} + l_{\text{rms}}/2$ .

importantly, a remarkable observation is that the collapse of PDF( $l$ ) exhibits a power-law behavior:

$$\text{PDF}(l) \sim l^\zeta. \quad (9)$$

The power-law scaling has an overall exponent equal to  $\zeta \approx -\frac{4}{3}$ , which is in very good agreement with the values reported in previous studies on canonical TBLs (e.g., Refs. [63,66–68]). Under all the tripping effects, the power-law behavior is almost independent of the intermittency parameter and the Reynolds number. Note that the power-law scaling almost ceases below the inner cutoff scale of  $\lambda_T$  like that reported by Chauhan *et al.* [68]. The outer cutoff is approximately at the scale of  $l_{\text{mean}} + l_{\text{rms}}/2$ , where  $l_{\text{mean}}$  and  $l_{\text{rms}}$  are the mean and RMS values of the segments  $l$  [69]. As shown, the data between the inner and outer cutoffs are marked by square symbols, which exhibit the power-law scaling over one order of magnitude of scale separation.

To explain the power-law scaling behavior in Fig. 17, we revisit the description of the fractal geometry of the instantaneous TNTI [63]. Following the additive properties of dimensions governing the intersection of fractals [70], the set of isolated TNTI points can be acquired from the one-dimensional hot-wire datasets, which are analogous to the Cantor's discontinuum and have the fractal dimension  $D_1$  with the relation:

$$D_3 = 2 + D_1, \quad (10)$$

where  $D_3$  is the fractal dimension of the TNTI in three-dimensional space. A box-counting algorithm has been widely used to obtain the fractal dimension from the one-dimensional hot-wire dataset. It is suggested that the number of boxes  $N(r)$  of size  $r$  cover a set of TNTI surface points, according to the relation:

$$N(r) \sim r^{-D_1}. \quad (11)$$

The TNTI interface is described to be fractallike only in an intermediate range. In this paper, the scale range between  $\lambda_T$  and  $l_{\text{mean}} + l_{\text{rms}}/2$  is considered. By systematically revealing the fractal facets of turbulence, Sreenivasan and Meneveau [71] pointed out that, due to the practical circumstances, there are no restrictive situations on scale cutoffs of the intermediate range. In this paper, the inner cutoff occurs at Taylor microscale  $\lambda_T$ , due to the relatively coarse resolution of the hot-wire sensor, whose spatial length is larger than the Kolmogorov scales. The finite resolution means that, as the TNTI area is measured by covering it with increasingly finer boxes, once the resolution of  $\lambda_T$  is reached, the convolutions on even finer scales no longer exist, and the TNTI area does not increase anymore.

In Fig. 18, the scale range with the power law of  $N(r) \sim r^{-D_1}$  is bounded by cutoffs on both ends. The exponent is approximately  $D_1 \approx 0.35$ . Following the relation in Eq. (10), it can be deduced that the fractal dimension of the TNTI is  $D_3 = 2 + D_1 \approx 2.35$ , which is matched with



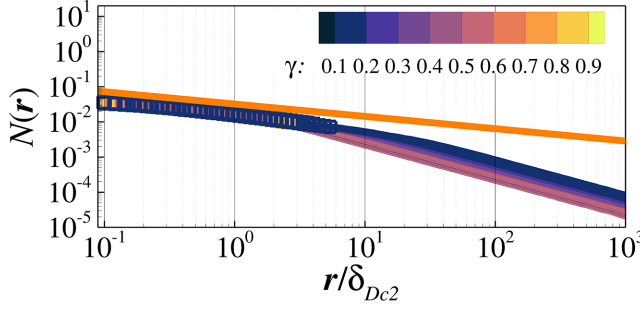


FIG. 18. The distribution of the number of boxes  $N(r)$  in the size of  $r$  covering the line intersection points of the turbulent/nonturbulent interface (TNTI) at the wall-normal heights in the range of  $0.1 \leq \gamma(y) \leq 0.9$ , under all the tripping conditions for case H. The solid yellow line indicates an exponential distribution with a one-dimensional fractal dimension  $D_1 \approx 0.35$ . The square symbols represent the intermediate range between  $\lambda_T$  and  $l_{\text{mean}} + l_{\text{rms}}/2$ .

the proposed value  $D_3 = 2.35 \pm 0.05$  in TBL flows [66]. Importantly, the result of  $D_1 \approx 0.35$  is sensibly independent of the intermittency factor  $0.1 \leq \gamma(y) \leq 0.9$  in all the current tripping conditions. Furthermore, from the viewpoint of probability statistics, PDF( $l$ ) pertains to the fractal set with the linear interactions and follows the power law [70]:

$$\text{PDF}(l) \sim l^{-D_1-1}, \quad (12)$$

which establishes a connection between the results of probability density and fractal dimension. As shown in Figs. 17 and 18, it provides the equation of  $-(D_1 + 1) = \zeta \approx -\frac{4}{3}$ , where  $D_1 \approx 0.35$ . Therefore, it can be concluded that, for the current artificially thickened TBLs introduced by the current trip wires, the intermittent geometry of the TNTI exhibits a fractallike self-similar convolution behavior within the intermediate scale range.

## VI. CONCLUSIONS

Single-point hot-wire anemometry has been performed at a given streamwise location in artificially thickened TBL flows generated by the trip wires of varying diameters. The trip wires with incremental diameters were employed as the tripping device. The experiment provided comprehensive insight into the impact of the trip wires with varying diameters on boundary layer flows from understimulation to overstimulation.

With increasing the diameter, the trip wire has a significant modification on the boundary layer, particularly in the outer region, as supported by the basic statistics, such as the mean flow, broadband turbulence intensities, and higher-order moments. The larger trip-wire diameter results in larger deviations of the TBL from canonical behavior. The wake region gradually disappears with increasing the diameter (namely, increasing the boundary-layer thickness and the Reynolds number). The spectra comparisons indicate that the overtripped conditions introduce large-scale perturbation into the boundary layer. These large-scale disturbances predominantly reside in the outer part and probably originate from the shedding of the trip-wire wake, akin to the wake behind the threaded rods from Marusic *et al.* [10]. The presence of such energetic motions is associated with the outer peak in the spectrogram, exhibiting a distinct separation from the inner peak. Through high-pass filtering, the disparities between the profiles of  $u_{\text{rms}}^+$  and  $S_u$  at various free-stream velocities and the tripping conditions are shown to mainly originate from the large-scale motions performing a direct interaction with the small scales. More importantly, it was indicated that the free-stream velocity is a dominant influence parameter in determining the turbulence statistics, in addition to the tripping diameter.

The trips broaden the inner spectral peak with contributions from larger scales, like those present in the outer peak. This refers to the effect that the generated large scales penetrate down to the wall, resulting in an increased near-wall peak in the broadband turbulence intensity based on the footprint effect [3,6,7]. In addition to the superposition of large-scale energy in the near-wall region, the AM effect was revealed by the cross-term of the scale-decomposed skewness factor  $3\overline{u_L^+ u_S^{+2}}$ . It was manifested that, as the large scales become more energetic with increasing the trip-wire diameter, their AM effect on the small scales is enhanced in the near-wall region. On the other hand, the zero-crossing-based approach was developed to describe the FM effect. The overall results indicate that the FM effects of the energetic large-scale structures on the small scales occur in the near-wall region, and the FM extent is strengthened by increasing  $D_c$ . In consideration of the effect of free-stream velocity, the comparison of the modulation profiles manifests that the free-stream velocity and tripping diameter are the two important factors to influence the near-wall AM and FM behavior. In addition, a reversal in both the AM and FM mechanisms was noted far away from the wall. The reversal becomes more noticeable, as the outer-layer intermittency is modified by the new-generated large scales.

Moreover, it was affirmed that the trip wire with increasing  $D_c$  leads to more thickened intermittent zones and greater tortuosity of the TNTI. The similar behavior of the outer-layer intermittency was noted, which is independent of the current tripping conditions. The PDFs of the length of the turbulent and nonturbulent segments  $l$  present a power-law behavior with an exponent of  $\zeta \approx -\frac{4}{3}$  for all the tripping conditions, which is in very good agreement with the value reported in canonical TBL [63,66–68,72]. Based on the linear intersection of TNTI with the stationary hot-wire probe measurements, a box-counting algorithm returns the TNTI fractal dimension of  $D_1 \approx 0.35$ . From the viewpoint of probability statistics, the relation of  $\text{PDF}(l)$  and the fractal dimension provide the equation of  $-(D_1 + 1) = \zeta \approx -\frac{4}{3}$ , where  $D_1 \approx 0.35$ . Thus, it was revealed that, under all the tripping effects, the random intermittent geometry of the TNTI exhibits a fractallike self-similar convolution behavior, within the intermediate scale range between the inner cutoff scale of the Taylor microscale  $\lambda_T$  and the outer cutoff scale of  $l_{\text{mean}} + l_{\text{rms}}/2$ . Importantly, this fractallike self-similar behavior is established across the entire intermittent zone, which is independent of the wall-normal position with the intermittency factor ranging from  $0.1 \leq \gamma(y) \leq 0.9$ .

In addition, in this paper, we underscore the necessity of caution when employing artificially thickened TBLs induced by leading-edge trips to simulate high- $\text{Re}_\tau$  TBLs within a finite-length test section. Within the range of free-streamwise velocities  $U_\infty \approx 5\text{--}13$  m/s, it is suggested that a tripping diameter of  $D_c \approx 2$  mm is optimal for generating canonical TBLs from a streamwise location  $x \gtrsim 1.4$ . The trip wires with smaller diameters tend to induce undertripped boundary layer flow, while larger trip wires result in artificially thickened TBLs in an overtripped status, with their statistical deviation from canonical TBLs becoming more distinct with increasing  $D_c$ , indicating the necessity of a longer streamwise distance for achieving canonical status. Essentially, larger  $D_c$  trip wires introduce large-scale structures into the boundary layers through the wake-driven mechanism owing to the 100% blockage of the trips at the wall [15]. The emergence of these large scales leads to a thicker boundary layer by exhibiting a wider external intermittent region, resulting in noncanonical behavior. The large-scale structures induced from the trip wires possess relatively longer wavelengths ( $\lambda_L^+$ ) at higher wall normal heights ( $y_L^+$ ) than VLSMs in canonical TBLs. Their energy and the derivatives of  $y_L^+$  and  $\lambda_L^+$  exhibit an overall increasing trend with  $D_c$ . These generated large-scale structures not only dominate in the outer layer but also influence near-wall turbulence through the footprint effect and AM/FM effect, presenting an increased inner peak and AM/FM extent with increasing  $D_c$ . The increased degree of both AM and FM effects is nearly up to 40% in the most overtripped cases. All the above observations suggest that the artificially thickened TBLs have the potential to simulate high- $\text{Re}_\tau$  TBLs. Nevertheless, it does not imply that artificially thickened TBLs are a reasonable approach to generating high- $\text{Re}_\tau$  canonical TBLs. A noticeable discrepancy can be observed in the high-order statistics and degree of AM/FM effects among artificially thickened cases at the nominally matched  $\text{Re}_\tau$ . Furthermore, to obtain a

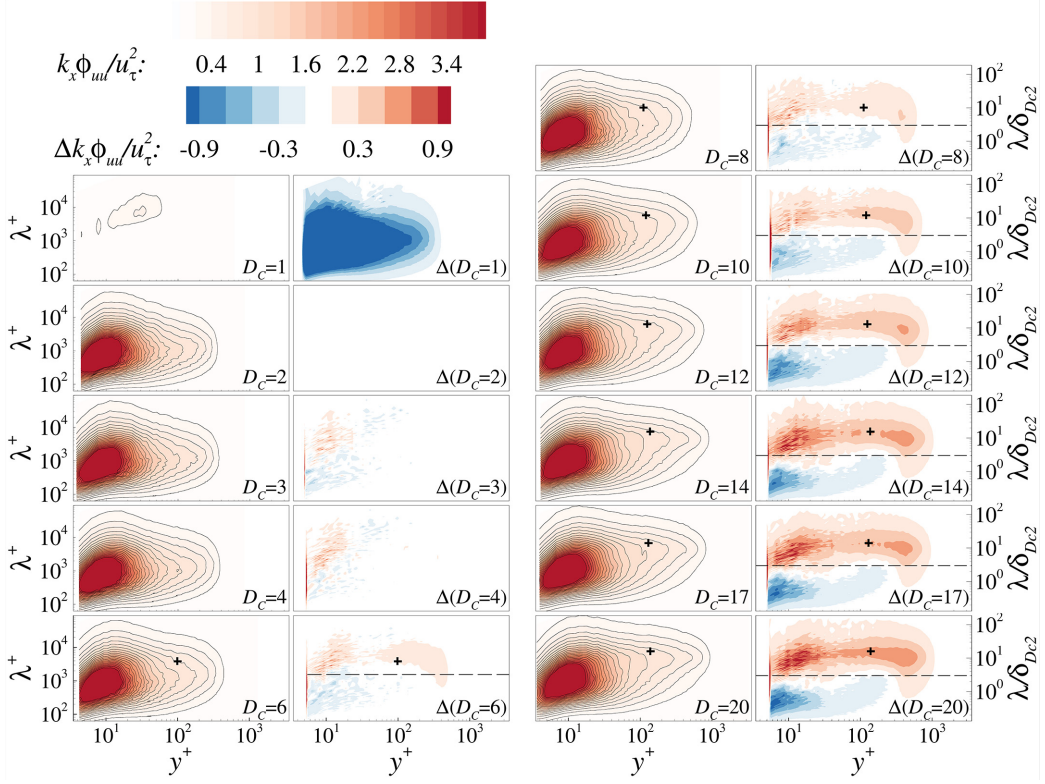


FIG. 19. Premultiplied spectra of the streamwise fluctuation signal for the different tripping conditions at low free-stream speed (case L). The details are consistent with that shown in Fig. 4.

high- $Re_\tau$  canonical TBL at a given free-stream velocity by thickening the boundary layer thickness, a decreasing trend of skin friction coefficient  $C_f$  with increasing  $D_c$  is expected. However, the friction coefficient  $C_f$  remains nearly constant for various  $D_c$  in this paper, which confirms that the artificially thickened TBLs are not canonical. The conclusions suggest that the observation of canonical behaviors, such as flow statistics, turbulent structure, and scale interactions, should be conducted in canonical TBL flows. In conclusion, pursuing excessive thickening of the boundary layer requires careful consideration, at least based on the current trip geometry, for generating high- $Re_\tau$  canonical TBLs in a finite-length test section, as a longer development region is necessary for the recovery of canonical properties with larger tripping diameters.

#### ACKNOWLEDGMENTS

The authors wish to gratefully acknowledge the National Natural Science Foundation of China (Grants No. 12272265, No. 12332017, and No. 12202310) and Chinesisch-Deutsche Zentrum für Wissenschaftsförderung (Grant No. GZ1575) for financial support. We would also like to give special thanks to Y. Huang for helpful discussions on the content of the manuscript.

#### APPENDIX: PREMULIPLIED SPECTRA

The premultiplied spectra of streamwise fluctuations  $k_x \phi_{uu}/u_\tau^2$  for each of the trip wire at the free-stream speed in cases L and M are shown in Figs. 19 and 20. They present consistent results with those shown in Fig. 4. As shown, the premultiplied spectra in the outer region exhibit enhanced

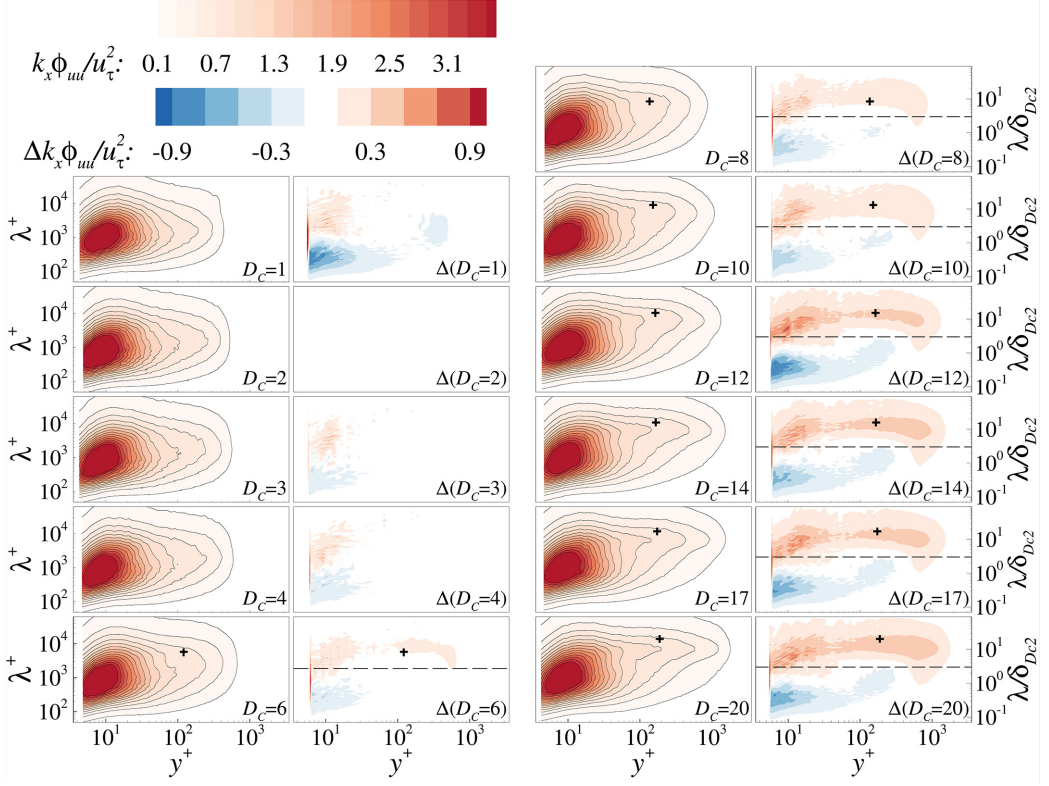


FIG. 20. Premultiplied spectra of the streamwise fluctuation signal for the different tripping conditions at medium free-stream speed (case M). The details are consistent with that shown in Fig. 4.

magnitudes with longer wavelengths at higher wall-normal locations, corresponding to an increase in the trip-wire diameter. The emergence of the large-scale energy is confirmed by the discrepancy map for the composite spectra, which shows the clear scale separation from the inner small scales, as marked by the dashed lines with  $\lambda_x/\delta_{D_c2} = 3$ . Moreover, in the overstimulated cases, the emergent large scales penetrate all the way down to the wall, confirming their presence throughout the boundary layer.

- 
- [1] A. J. Smits, B. J. McKeon, and I. Marusic, High-Reynolds number wall turbulence, *Annu. Rev. Fluid Mech.* **43**, 353 (2011).
  - [2] I. Marusic, B. J. McKeon, P. A. Monkewitz, H. M. Nagib, A. J. Smits, and K. R. Sreenivasan, Wall-bounded turbulent flows at high Reynolds numbers: Recent advances and key issues, *Phys. Fluids* **22**, 065103 (2010).
  - [3] N. Hutchins and I. Marusic, Large-scale influences in near-wall turbulence, *Phil. Trans. R. Soc. A* **365**, 647 (2007).
  - [4] A. Andreolli, D. Gatti, R. Vinuesa, R. Örlü, and P. Schlatter, Separating large-scale superposition and modulation in turbulent channels, *J. Fluid Mech.* **958**, A37 (2023).
  - [5] N. Hutchins and I. Marusic, Evidence of very long meandering features in the logarithmic region of turbulent boundary layers, *J. Fluid Mech.* **579**, 1 (2007).

- [6] W. J. Baars, N. Hutchins, and I. Marusic, Reynolds number trend of hierarchies and scale interactions in turbulent boundary layers, *Phil. Trans. R. Soc. A* **375**, 20160077 (2017).
- [7] B. Ganapathisubramani, N. Hutchins, J. P. Monty, D. Chung, and I. Marusic, Amplitude and frequency modulation in wall turbulence, *J. Fluid Mech.* **712**, 61 (2012).
- [8] R. Mathis, N. Hutchins, and I. Marusic, Large-scale amplitude modulation of the small-scale structures in turbulent boundary layers, *J. Fluid Mech.* **628**, 311 (2009).
- [9] E. Dogan, R. Örlü, D. Gatti, R. Vinuesa, and P. Schlatter, Quantification of amplitude modulation in wall-bounded turbulence, *Fluid Dyn. Res.* **51**, 011408 (2019).
- [10] I. Marusic, K. A. Chauhan, V. Kulandaivelu, and N. Hutchins, Evolution of zero-pressure-gradient boundary layers from different tripping conditions, *J. Fluid Mech.* **783**, 379 (2015).
- [11] P. S. Klebanoff and Z. W. Diehl, Some features of artificially thickened fully developed turbulent boundary layers with zero pressure gradient, Tech. Rep. No. NACA-TR-1110, 1952.
- [12] P. Schlatter and R. Örlü, Turbulent boundary layers at moderate Reynolds numbers: Inflow length and tripping effects, *J. Fluid Mech.* **710**, 5 (2012).
- [13] P. Schlatter and R. Örlü, Assessment of direct numerical simulation data of turbulent boundary layers, *J. Fluid Mech.* **659**, 116 (2010).
- [14] L. P. Erm and P. N. Joubert, Low-Reynolds-number turbulent boundary layers, *J. Fluid Mech.* **230**, 1 (1991).
- [15] E. Rodríguez-López, P. J. K. Bruce, and O. R. H. Buxton, On the formation mechanisms of artificially generated high Reynolds number turbulent boundary layers, *Boundary Layer Meteorol.* **160**, 201 (2016).
- [16] O. R. H. Buxton, M. Ewenz Rocher, and E. Rodríguez-López, Influence of strong perturbations on wall-bounded flows, *Phys. Rev. Fluids* **3**, 014605 (2018).
- [17] E. Rodríguez-López, P. J. K. Bruce, and O. R. H. Buxton, Flow characteristics and scaling past highly porous wall-mounted fences, *Phys. Fluids* **29**, 075106 (2017).
- [18] C. Sanmiguel Vila, R. Vinuesa, S. Discetti, A. Ianaro, P. Schlatter, and R. Örlü, On the identification of well-behaved turbulent boundary layers, *J. Fluid Mech.* **822**, 109 (2017).
- [19] Z. Tang, X. Ma, N. Jiang, X. Cui, and X. Zheng, Local dynamic perturbation effects on the scale interactions in wall turbulence, *J. Turbul.* **22**, 208 (2020).
- [20] Z. Tang and N. Jiang, Scale interaction and arrangement in a turbulent boundary layer perturbed by a wall-mounted cylindrical element, *Phys. Fluids* **30**, 055103 (2018).
- [21] Z. Tang, N. Jiang, X. Zheng, and Y. Wu, Bursting process of large- and small-scale structures in turbulent boundary layer perturbed by a cylinder roughness element, *Exp. Fluids* **57**, 79 (2016).
- [22] P. M. Ligrani and P. Bradshaw, Spatial resolution and measurement of turbulence in the viscous sublayer using subminiature hot-wire probes, *Exp. Fluids* **5**, 407 (1987).
- [23] N. Hutchins, T. B. Nickels, I. Marusic, and M. S. Chong, Hot-wire spatial resolution issues in wall-bounded turbulence, *J. Fluid Mech.* **635**, 103 (2009).
- [24] N. Hutchins, J. P. Monty, M. Hultmark, and A. J. Smits, A direct measure of the frequency response of hot-wire anemometers: Temporal resolution issues in wall-bounded turbulence, *Exp. Fluids* **56**, 18 (2015).
- [25] E. Rodríguez-López, P. J. K. Bruce, and O. R. H. Buxton, A robust post-processing method to determine skin friction in turbulent boundary layers from the velocity profile, *Exp. Fluids* **56**, 68 (2015).
- [26] P. A. Monkewitz, K. A. Chauhan, and H. M. Nagib, Self-consistent high-Reynolds-number asymptotics for zero-pressure-gradient turbulent boundary layers, *Phys. Fluids* **19**, 115101 (2007).
- [27] D. Coles, The law of the wake in the turbulent boundary layer, *J. Fluid Mech.* **1**, 191 (1956).
- [28] K. A. Chauhan, P. A. Monkewitz, and H. M. Nagib, Criteria for assessing experiments in zero pressure gradient boundary layers, *Fluid Dyn. Res.* **41**, 021404 (2009).
- [29] S. C. C. Bailey, M. Hultmark, J. P. Monty, P. H. Alfredsson, M. S. Chong, R. D. Duncan, J. H. M. Fransson, N. Hutchins, I. Marusic, B. J. McKeon *et al.*, Obtaining accurate mean velocity measurements in high Reynolds number turbulent boundary layers using Pitot tubes, *J. Fluid Mech.* **715**, 642 (2013).
- [30] A. J. Musker, Explicit expression for the smooth wall velocity distribution in a turbulent boundary layer, *AIAA J.* **17**, 655 (1979).



- [31] I. Marusic, J. P. Monty, M. Hultmark, and A. J. Smits, On the logarithmic region in wall turbulence, *J. Fluid Mech.* **716**, R3 (2013).
- [32] H. M. Nagib and K. A. Chauhan, Variations of von Kármán coefficient in canonical flows, *Phys. Fluids* **20**, 101518 (2008).
- [33] A. Segalini, R. Örlü, and P. H. Alfredsson, Uncertainty analysis of the von Kármán constant, *Exp. Fluids* **54**, 1460 (2013).
- [34] E. Rodríguez-López, P. J. K. Bruce, and O. R. H. Buxton, Near field development of artificially generated high Reynolds number turbulent boundary layers, *Phys. Rev. Fluids* **1**, 074401 (2016).
- [35] E. Dogan, R. E. Hanson, and B. Ganapathisubramani, Interactions of large-scale free-stream turbulence with turbulent boundary layers, *J. Fluid Mech.* **802**, 79 (2016).
- [36] Y. Jooss, L. Li, T. Bracchi, and R. J. Hearst, Spatial development of a turbulent boundary layer subjected to freestream turbulence, *J. Fluid Mech.* **911**, A4 (2021).
- [37] A. J. Smits, J. Monty, M. Hultmark, S. C. C. Bailey, N. Hutchins, and I. Marusic, Spatial resolution correction for wall-bounded turbulence measurements, *J. Fluid Mech.* **676**, 41 (2011).
- [38] R. Örlü and P. H. Alfredsson, On spatial resolution issues related to time-averaged quantities using hot-wire anemometry, *Exp. Fluids* **49**, 101 (2010).
- [39] O. M. Phillips, The irrotational motion outside a free turbulent boundary, *Math. Proc. Cambridge Philos. Soc.* **51**, 220 (1955).
- [40] M. M. Metzger and J. C. Klewicki, A comparative study of near-wall turbulence in high and low Reynolds number boundary layers, *Phys. Fluids* **13**, 692 (2001).
- [41] R. Mathis, I. Marusic, N. Hutchins, and K. R. Sreenivasan, The relationship between the velocity skewness and the amplitude modulation of the small scale by the large scale in turbulent boundary layers, *Phys. Fluids* **23**, 121702 (2011).
- [42] Z. Tang, L. Chen, Z. Fan, X. Ma, and N. Jiang, Cross-term events of scale-decomposed skewness factor in turbulent boundary layer at moderate Reynolds number, *Phys. Fluids* **33**, 055124 (2021).
- [43] P. Schlatter and R. Örlü, Quantifying the interaction between large and small scales in wall-bounded turbulent flows: A note of caution, *Phys. Fluids* **22**, 051704 (2010).
- [44] D. Chung and B. J. McKeon, Large-eddy simulation of large-scale structures in long channel flow, *J. Fluid Mech.* **661**, 341 (2010).
- [45] W. J. Baars, K. M. Talluru, N. Hutchins, and I. Marusic, Wavelet analysis of wall turbulence to study large-scale modulation of small scales, *Exp. Fluids* **56**, 188 (2015).
- [46] G. Iacobello, L. Ridolfi, and S. Scarsoglio, Large-to-small scale frequency modulation analysis in wall-bounded turbulence via visibility networks, *J. Fluid Mech.* **918**, A13 (2021).
- [47] G. Pathikonda and K. T. Christensen, Inner-outer interactions in a turbulent boundary layer overlying complex roughness, *Phys. Rev. Fluids* **2**, 044603 (2017).
- [48] A. Awasthi and W. Anderson, Numerical study of turbulent channel flow perturbed by spanwise topographic heterogeneity: Amplitude and frequency modulation within low- and high-momentum pathways, *Phys. Rev. Fluids* **3**, 044602 (2018).
- [49] Z. Tang, Z. Fan, L. Chen, and N. Jiang, Outer-layer structure arrangements based on the large-scale zero-crossings at moderate Reynolds number, *Phys. Fluids* **33**, 085121 (2021).
- [50] J. Eisma, J. Westerweel, G. Ooms, and G. E. Elsinga, Interfaces and internal layers in a turbulent boundary layer, *Phys. Fluids* **27**, 055103 (2015).
- [51] K. R. Sreenivasan, A. Prabhu, and R. Narasimha, Zero-crossings in turbulent signals, *J. Fluid Mech.* **137**, 251 (1983).
- [52] B. Boashash, *Time-Frequency Signal Analysis and Processing: A Comprehensive Reference* (Academic Press, London, 2015).
- [53] L. Agostini and M. Leschziner, On the departure of near-wall turbulence from the quasi-steady state, *J. Fluid Mech.* **871**, R1 (2019).
- [54] S. Corrsin and A. L. Kistler, Free-stream boundaries of turbulent flows, Tech. Rep. No. NACA-TR-1244, 1955.
- [55] D. K. Bisset, J. C. R. Hunt, and M. M. Rogers, The turbulent/non-turbulent interface bounding a far wake, *J. Fluid Mech.* **451**, 383 (2002).

- [56] G. Borrell and J. Jiménez, Properties of the turbulent/non-turbulent interface in boundary layers, *J. Fluid Mech.* **801**, 554 (2016).
- [57] K. Chauhan, J. Philip, C. M. de Silva, N. Hutchins, and I. Marusic, The turbulent/non-turbulent interface and entrainment in a boundary layer, *J. Fluid Mech.* **742**, 119 (2014).
- [58] N. Reuther and C. J. Kähler, Evaluation of large-scale turbulent/non-turbulent interface detection methods for wall-bounded flows, *Exp. Fluids* **59**, 121 (2018).
- [59] K. Younes, B. Gibeau, S. Ghaemi, and J.-P. Hickey, A fuzzy cluster method for turbulent/non-turbulent interface detection, *Exp. Fluids* **62**, 73 (2021).
- [60] Y. Long, D. Wu, and J. Wang, A novel and robust method for the turbulent/non-turbulent interface detection, *Exp. Fluids* **62**, 138 (2021).
- [61] T. Saxton-Fox and B. J. McKeon, Coherent structures, uniform momentum zones and the streamwise energy spectrum in wall-bounded turbulent flows, *J. Fluid Mech.* **826**, R6 (2017).
- [62] L. Chen, Z. Fan, Z. Tang, X. Wang, D. Shi, and N. Jiang, Outer-layer coherent structures from the turbulent/non-turbulent interface perspective at moderate Reynolds number, *Exp. Therm Fluid Sci.* **140**, 110760 (2023).
- [63] C. M. de Silva, J. Philip, K. Chauhan, C. Meneveau, and I. Marusic, Multiscale geometry and scaling of the turbulent-nonturbulent interface in high Reynolds number boundary layers, *Phys. Rev. Lett.* **111**, 044501 (2013).
- [64] P. S. Klebanoff, Characteristics of turbulence in a boundary layer with zero pressure gradient, Tech. Rep. No. NACA-TR-1247, 1955.
- [65] T. B. Hedley and J. F. Keffer, Some turbulent/non-turbulent properties of the outer intermittent region of a boundary layer, *J. Fluid Mech.* **64**, 645 (1974).
- [66] K. R. Sreenivasan, R. Ramshankar, and C. Meneveau, Mixing, entrainment and fractal dimensions of surfaces in turbulent flows, *Proc. R. Soc. Lond. A* **421**, 79 (1989).
- [67] C. Meneveau and K. R. Sreenivasan, Interface dimension in intermittent turbulence, *Phys. Rev. A* **41**, 2246 (1990).
- [68] K. A. Chauhan, R. Baidya, J. Philip, N. Hutchins, and I. Marusic, Intermittency in the outer region of turbulent boundary layers, in *19th Australasian Fluid Mechanics Conference* (RMIT University, Melbourne, Australia, 2014).
- [69] Y. Tsuji and I. Nakamura, The fractal aspect of an isovelocity set and its relationship to bursting phenomena in the turbulent boundary layer, *Phys. Fluids* **6**, 3429 (1994).
- [70] B. B. Mandelbrot, *The Fractal Geometry of Nature* (W. H. Freeman and Co., San Francisco, 1982), p. 460.
- [71] K. R. Sreenivasan and C. Meneveau, The fractal facets of turbulence, *J. Fluid Mech.* **173**, 357 (1986).
- [72] Y. Tsuji, K. Honda, I. Nakamura, and S. Sato, Is intermittent motion of outer flow in the turbulent boundary layer deterministic chaos? *Phys. Fluids A* **3**, 1941 (1991).